

# THE OBSERVATORY

---

Vol. 144

2024 FEBRUARY

No. 1298

---

## ESTIMATION OF VISUAL-BINARY ORBITAL ELEMENTS UTILIZING OPTIMAL CURVE-FITTING PROCEDURES

By M. D. Rhodes<sup>1</sup>, T. S. Banks<sup>2</sup>, E. Budding<sup>3</sup> & T. Love<sup>4</sup>

<sup>1</sup>Brigham Young University, Utah, USA

<sup>2</sup>Dept. of Physical Science & Engineering, Harper College, USA

<sup>3</sup>Carter Observatory, Wellington, New Zealand

<sup>4</sup>Variable Stars South, Wellington, New Zealand

We demonstrate optimal curve-fitting procedures to the parametrization of a selection of 25 visual-binary-star orbits from F. W. Dyson's<sup>1</sup> catalogue. We compare our findings with other published results, which reveal uncertainties, real and formal, affecting the parameters. The extent of data coverage for any one system can have a substantial impact on the modelled results, with various orbital solutions sometimes possible for a single system.

### *Introduction*

Comparative study of the properties of binary stars started in the late-18th Century, notably with the work of the Herschel family. In his classic review of wide double stars, W. Herschel<sup>2</sup> was able to confirm Newtonian gravity as the agent for their apparent motions in Keplerian ellipses. Visual binaries at known distances are thus able to reveal useful physical characteristics of stars, namely their masses and luminosities. However, the proportion of visual binaries for which elliptic orbital motion was clearly established has been low, usually involving periods of up to just a few hundred years, *i.e.*, separations of a few score AU.

### *Background*

To scale the observed angular separation on the sky of the two components of a visual binary to absolute units, it is necessary to know the system's mean parallax. Historically, this was difficult to derive with high accuracy, even for the nearest stars<sup>3-5</sup>. This point has limited the extent to which the astrometry of visual pairs could bear on general astrophysics until relatively recent times. Even though there may be a few-hundred binaries with parallaxes greater than 0.1 arcsec, such is the increase in numbers of stars of low mass that ~90% of this

nearby population would be made up of stars with less than half the mass of the Sun. Increased precision of double-star data, including parallaxes, obtained from modern space-based platforms is likely to change this perspective considerably over coming years<sup>6</sup>. The present juncture offers opportunities to look back over historical data and check on methods for accurate parametrization of datasets.

The elliptical form of an orbit is written in the standard arrangement as given by Smart<sup>7</sup>:

$$Ax^2 + 2Hxy + By^2 + 2Gx + 2Fy + 1 = 0. \quad (1)$$

The essence of the inverse problem for the visual-binary orbit is to relate the five coefficients  $A-H$  to the five regular orbital parameters  $a$ ,  $e$ ,  $i$ ,  $\omega$ , and  $\Omega$ . The values of  $A-H$  can be derived from an appropriate selection of  $x$  and  $y$  values on the observed ellipse. Meanwhile, the orbital parameters in their own natural frame of reference  $(\xi, \eta)$  of reference, centred on the primary focus, satisfy

$$\frac{(\xi + ae)^2}{a^2} + \frac{\eta^2}{a^2(1 - e^2)} = 1. \quad (2)$$

This would correspond directly with the apparent orbit only in the 'face-on' conditions that  $\Omega = \pi/2$ ,  $i$  and  $\omega = 0$ . In general, these three 'Eulerian' angles are associated with coordinate rotations about, progressively, the  $z$ ,  $x$ , and  $z$  (again) axes, with the result that for a point on the orbit where the true anomaly is  $v$ , the  $x$ ,  $y$ , and  $z$  (*i.e.*, line of sight) coordinates satisfy the following equations<sup>8</sup>:

$$\begin{aligned} x &= \frac{a(1 - e^2)}{(1 + e \cos v)} [\cos(v + \omega) \sin \Omega + \sin(v + \omega) \cos \Omega \cos i], \\ y &= \frac{a(1 - e^2)}{(1 + e \cos v)} [\cos(v + \omega) \cos \Omega - \sin(v + \omega) \sin \Omega \cos i], \\ z &= \frac{a(1 - e^2)}{(1 + e \cos v)} \sin(v + \omega) \sin i. \end{aligned} \quad (3)$$

Various methods exist to relate the five constants in (1) to those in (3).

Classical methods involve reversing the three rotational coordinate transformations that gave rise to (3) from the natural, un-rotated, forms for  $\xi$  and  $\eta$ . The set of equations (3) is inverted to find forms for  $\xi$  and  $\eta$  in terms of  $x$  and  $y$ . These can be substituted into (2) and then comparison of the terms in  $x^2$ ,  $xy$ ,  $y^2$ , *etc.*, allow the relations between the five observationally derived coefficients  $A-H$  to be related to the parameters  $a-\Omega$ . There are still the two time-related parameters that fix the position of the secondary with respect to the primary for any particular time, namely the orbital period  $P$  and reference epoch  $T_0$ . A pair of points on the ellipse, at known times, are sufficient to derive these, their true anomaly values being determined from (3) with the known geometric parameters. Both these  $v$  values have a corresponding mean anomaly, which, taken together, fix the values of  $P$  and  $T_0$ .

With the use of modern computers, it becomes easily practicable to deal with the parametrization of the fitting function by programmed optimization methods. Instead of carrying out linear operations with  $A-H$  determined from selected points on the apparent orbit, the ellipse that corresponds to (2) is

progressively matched to the full  $x$  and  $y$  datasets to minimize residuals.

The fitting functions will contain the full seven constants discussed above, as well as small fiducial corrections,  $\Delta x_0$ ,  $\Delta y_0$ , in the position to be assigned to the origin. Formally, we can write for the solution of the inverse problem set out in this way<sup>9,10</sup>:

$$\mathbf{a}_{\text{opt}} = [\chi^2]^{-1} \text{Min}[\chi^2(\mathbf{a})], \quad (4)$$

where  $\mathbf{a}_{\text{opt}}$  is the vector of best estimates of each parameter in the adjustable set  $\{a_1, a_2, a_3, \dots, a_j, \dots, a_m\}$ . The observed values of the variable, either  $x$  or  $y$ , or both, are matched by the values of the fitting function, calculated from (3). The  $z$  values, that may be available in certain cases, can be treated in the same way.

The quantity  $\chi^2$  depends on the squared differences of observed and calculated quantities, and the optimal estimate for each  $a_i$  is taken to occur when  $\chi^2$  is minimized. The quantity  $[\chi^2]^{-1}$  expresses the idea of inversion of the dependence of  $\chi^2$  on  $\mathbf{a}$ . Posed in this way, parametrization of the orbit model becomes a standard optimization problem. The inversion can be regarded as a guided trial-and-error process, in which exploration of the  $(\chi^2, \mathbf{a})$  hypersurface locates the appropriate minimum. The search direction is optimized by its alignment with the local gradient of the fitting function, and the extent of movement in this direction can be ascertained from a local grid-search. The well-known Levenberg–Marquardt procedure carries out these two operations in a suitably weighted combination<sup>11</sup>. The numerical value of the gradient (‘steepest descent’) applies to a short path-length in the  $(\chi^2, \mathbf{a})$  hypersurface, where we can regard the fitting function as the application of Eqns (3) to match the observations of the separation and position angle. This is effectively linearized as the leading terms in the corresponding Taylor series. Linearization of the fitting function is equivalent to a parabolization of the local  $(\chi^2, \mathbf{a})$  hypersurface. This will allow that grid-searching with small steps determines both the search direction, from the available conjugate axes of local  $(\chi^2, \mathbf{a})$  elliptical contours, and the distance to travel in that direction, *i.e.*, to the centre of such a contour<sup>12</sup>.

This is essentially the approach of Bevington’s<sup>13</sup> CHFIT program, where the position of, and direction to, the optimum are calculated from the behaviour of  $\chi^2$  in response to parameter variation. Convergence implies a Newton–Raphson closeness of priors to their posterior counterparts. This method has been implemented by the authors as FITASTROMETRY.

FITASTROMETRY is thus an inherently iterative procedure, continuing until fit improvements have fallen below a pre-set small quantity, if that happens before a pre-set maximum number of iterations. After each fourth iteration, in the current version, conjugate-axis and centring calculations are carried out to locate the current estimate of the  $\text{Min}(\chi^2, \mathbf{a})$  position. This combination of grid-search and elliptical contour fixing are usually productive for rapid orbit model parametrization. But occasionally we have the ‘long valley’ problem where a group of parameters are close to linear correlation, and the trend of model improvements becomes slow, or ineffective. An example of this was found in modelling the orbit of 36 And (WDS 00550+2338). This application is discussed below. The general usefulness of modelling procedures is circumscribed by the extent and accuracy of the orbital data. Uncertainties in the parametrization arise with observational scatter and limited coverage of the orbit.

Our main purposes in what follows are (i) to demonstrate optimal curve-fitting procedures to the parametrization of a selection of visual-binary-

star orbits from Dyson's catalogue; and (ii) to compare findings with other published results. This should reveal uncertainties, real and formal, affecting the parameters. Consequently, (iii) we offer updated quantities of physical interest. FITASTROMETRY is now an option in WINFITTER and freely available to researchers. Further information is given by Budding & Demircan.<sup>14</sup>

#### *Selection of data and method*

The work of Dyson and his colleagues<sup>1</sup> published in the section titled *Orbits of 25 Double Stars* represents a fairly complete and homogeneous data set. The observations span an interval from the early 1800s to 1921. Twenty-three orbit models were published by Jackson<sup>15</sup>. The system 73 Oph (WDS 18096+0400) was added later and BD+183182 (WDS 16289+1825) was recomputed including observations from the Yerkes Observatory. Such a data set was ideal for the purpose of testing FITASTROMETRY, with the added advantage that we had available an additional hundred years of data (sourced from the *Washington Double Star Catalogue*<sup>16</sup> courtesy of the USNO) compared to Dyson. We could therefore contrast solutions based on just the Dyson data with those including the more recent data, acting as an update and hopefully a validation of Dyson's work.

Table I summarizes the values of the orbital parameters of these 25 binary stars taken from Dyson (D), the *Washington Catalogue* (W), and the optimized values from the FITASTROMETRY program (F).

Table II summarizes the calculated values of the dynamical parallaxes using orbital parameters of the 25 binary stars taken from Dyson (D), the *Washington Catalogue* (W), and the optimized values from the FITASTROMETRY program. Parallax values obtained from the *Hipparcos* and *Gaia* satellite data are shown for comparison.

#### *Results and comparison with Dyson and WDS parameters*

We ran FITASTROMETRY on each of the 25 Dyson visual binaries, using the full data sets including the WDS data. In Table III we present only the results of the fitting for the first system, WDS 00550+2338 (36 And). Orbital plots from Dyson, WDS, and FITASTROMETRY are shown in Figs. 1, 2, and 3. An appendix maintained at <https://michaelrhodesbyu.weebly.com> contains the FITASTROMETRY findings for all 25 of the Dyson (1921) collection.

The final parameter estimates for the 25 systems from WDS and FITASTROMETRY are in close agreement, as demonstrated by the high correlation values (see Table IV) together with the gradient of these linear models being close to unity. However, the Dyson values differ significantly from WDS and FITASTROMETRY values, as shown by the  $R^2$  values for two selected parameters ( $i$  and  $\omega$ ). This significance was reduced by recognizing that Dyson restricted inclination values to be less than or equal to 90 degrees and that  $\omega$  be less than 180 degrees. These are ambiguities rather than actual errors since  $\omega + 180$  will produce the same result as  $\omega$ . Making these changes led to improved agreement between the solutions, as evidenced by the correlations shown in the column "WDS to adjusted Dyson" in Table IV. Once these adjustments were made, the agreement between WDS (and by proxy FITASTROMETRY) and Dyson's values is reasonable (see Figs. 4a and b), particularly given that Dyson's fits cover a shorter time period.

These systems have long periods, and in many cases Dyson's data had not covered a complete orbit. A more representative comparison against the Dyson parameter estimates is therefore to model only the data available to Dyson. Below are the results of following that procedure with the first Dyson binary, WDS 00550+2338. Table V shows the results using only the Dyson values of the orbital parameters and Table VI shows the result using the WDS values of the orbital parameters. Fig. 5 compares the orbital plots of the corresponding results.

TABLE I

*A comparison of the orbital elements given in Dyson's catalogue<sup>1</sup> (D), the Washington Double Star Catalogue<sup>16</sup> (W), and the FITASTROMETRY (F) optimized values of the 25 Dyson binary-orbit fittings. P is in Besselian years, a in arcseconds,  $\omega$ ,  $i$ , and  $\Omega$  are in degrees, and  $T_0$  is in decimal tropical years AD. The precision suggested by the number of digits retained after the decimal point slightly exceeds its real value.*

	P	a	e	$\omega$	i	$\Omega$	$T_0$
D-1	124.2	0.970	0.708	76.5	41.2	105.7	1816.9
W	167.4	0.984	0.306	358.6	44.6	173.7	1956.2
F	168.6	1.014	0.308	358.6	45.2	173.8	1956.3
D-2	167.4	0.974	0.313	303.7	61.3	99.7	1894.5
W	145.4	0.890	0.263	322.7	63.8	99.1	1899.1
F	145.0	0.844	0.254	326.0	60.8	99.6	1901.2
D-3	216.9	0.407	0.545	350.0	37.0	106.5	1919.4
W	522.2	0.625	0.679	238.1	157.2	13.0	1911.6
F	495.0	0.619	0.670	234.0	153.0	10.0	1912.0
D-4	95.2	0.440	0.050	174.8	58.2	55.3	1917.2
W	188.0	0.549	0.450	31.0	52.7	72.9	1887.0
F	189.0	0.568	0.430	32.0	57.0	74.0	1888.0
D-5	88.2	0.627	0.519	316.3	50.4	122.0	1882.9
W	98.0	0.743	0.592	312.3	50.3	142.6	1882.5
F	94.0	0.751	0.620	307.0	53.9	143.7	1982.0
D-6	59.6	0.350	0.611	114.9	74.6	35.2	1861.1
W	58.0	0.343	0.672	241.0	72.5	9.5	1944.2
F	57.0	0.326	0.680	236.0	69.0	7.0	1943.0
D-7	110.1	0.319	0.473	44.5	32.2	124.6	1883.6
W	104.6	0.329	0.436	33.2	19.4	132.5	1987.5
F	105.0	0.353	0.443	28.0	28.0	139.0	1987.0
D-8	361.0	1.000	0.926	59.1	43.6	78.4	1888.1
W	421.3	1.071	0.901	17.9	112.4	147.7	1892.9
F	486.0	1.130	0.909	14.0	131.0	146.0	1893.0
D-9	220.4	1.205	0.856	241.4	47.4	52.8	1860.3
W	245.0	1.111	0.833	140.0	160.0	65.0	1865.0
F	242.0	1.005	0.820	140.0	160.0	148.0	1863.0
D-10	193.6	2.549	0.460	180.5	39.4	156.3	1913.3
W	156.0	2.443	0.447	200.0	47.7	156.6	1916.7
F	157.0	2.438	0.446	199.0	47.2	155.8	1916.0

TABLE I (concluded)

	$P$	$a$	$e$	$\omega$	$i$	$\Omega$	$T_0$
D-11	238.0	1.060	0.700	208.6	57.6	74.1	1868.3
W	253.0	1.111	0.699	328.0	118.0	251.3	1866.0
F	250.0	1.100	0.700	327.0	117.0	251.0	1867.0
D-12	88.5	0.330	0.553	222.3	25.6	41.7	1882.6
W	89.0	0.327	0.523	171.0	165.0	71.0	2060.7
F	89.0	0.315	0.529	171.4	173.0	71.0	2061.0
D-13	234.8	1.271	0.560	23.1	40.9	174.5	1865.0
W	257.0	1.450	0.579	339.0	134.0	176.0	1894.0
F	261.0	1.466	0.591	336.0	135.0	173.0	1894.0
D-14	317.5	2.870	0.770	245.5	75.0	93.1	1920.2
W	229.0	2.231	0.758	131.0	108.3	94.3	1921.0
F	224.0	2.250	0.762	129.0	108.0	94.0	1921.0
D-15	110.0	1.328	0.860	96.7	53.2	110.0	1927.4
W	129.0	0.898	0.615	148.9	24.0	61.0	1939.5
F	129.0	0.951	0.611	149.0	25.2	61.0	1939.0
D-16	126.1	0.935	0.435	213.0	59.3	147.1	1894.5
W	120.0	0.975	0.418	149.7	118.2	145.6	1895.0
F	122.0	0.956	0.399	154.0	117.0	149.0	1894.0
D-17	154.5	0.783	0.387	316.7	34.2	0.6	1900.4
W	274.0	1.039	0.579	250.0	32.0	46.0	1896.2
F	267.0	1.013	0.567	243.0	31.2	53.0	1896.0
D-18							
W	88.0	0.278	0.653	12.3	57.3	146.4	1968.2
F	87.0	0.265	0.643	8.0	57.0	149.0	1968.0
D-19	423.5	1.330	0.700	60.1	73.7	71.1	1910.0
W	294.0	1.190	0.610	307.0	103.0	71.0	1912.8
F	288.0	1.151	0.620	305.0	102.9	71.0	1914.0
D-20	354.9	1.205	0.933	93.4	37.5	1.0	1887.3
W	510.0	1.424	0.886	352.0	122.0	98.0	1880.0
F	514.0	1.420	0.889	350.0	123.8	97.0	1880.0
D-21	321.0	2.120	0.188	159.0	47.8	87.9	1941.6
W	657.0	2.689	0.440	151.0	154.0	139.0	1866.0
F	626.0	2.540	0.406	152.0	164.0	138.0	1866.0
D-22	128.0	0.566	0.179	55.0	51.5	146.4	1946.7
W	178.0	0.688	0.081	41.2	129.4	152.2	1831.4
F	163.0	0.635	0.070	100.0	131.0	154.0	1951.0
D-23	151.7	0.695	0.375	59.7	67.4	167.8	1897.2
W	201.0	0.816	0.535	45.9	64.1	174.3	1897.0
F	199.0	0.834	0.522	45.0	64.8	175.1	1896.8
D-24	85.7	0.790	0.773	288.9	43.0	174.1	1904.7
W	97.0	0.743	0.770	287.0	27.0	177.0	1905.3
F	96.0	0.722	0.769	287.0	23.0	177.0	1905.0
D-25	40.8	0.500	0.350	114.2	69.7	119.1	1915.4
W	217.0	0.879	0.630	148.0	128.0	147.0	1903.0
F	264.0	0.885	0.656	148.0	128.0	145.0	1903.0

TABLE II

A comparison of the calculated dynamical parallaxes of the 25 Dyson binary stars utilizing the orbital elements given in Dyson's catalogue<sup>1</sup> (D), the Washington Double Star Catalogue<sup>16</sup> (W), and the FITASTROMETRY program (F) optimized values of the 25 Dyson binary-orbit parameters.  $P$  is in years,  $a$  in arcseconds. The two values of parallax  $\pi(H)$  and  $\pi(G)$  are in milliarcseconds (mas) and are taken from the Hipparcos catalogue<sup>17</sup> (H) and from the Gaia catalogue<sup>6</sup> (G). Note that the Gaia catalogue did not have values for several of the binary systems. The dynamical parallaxes are calculated using the formula

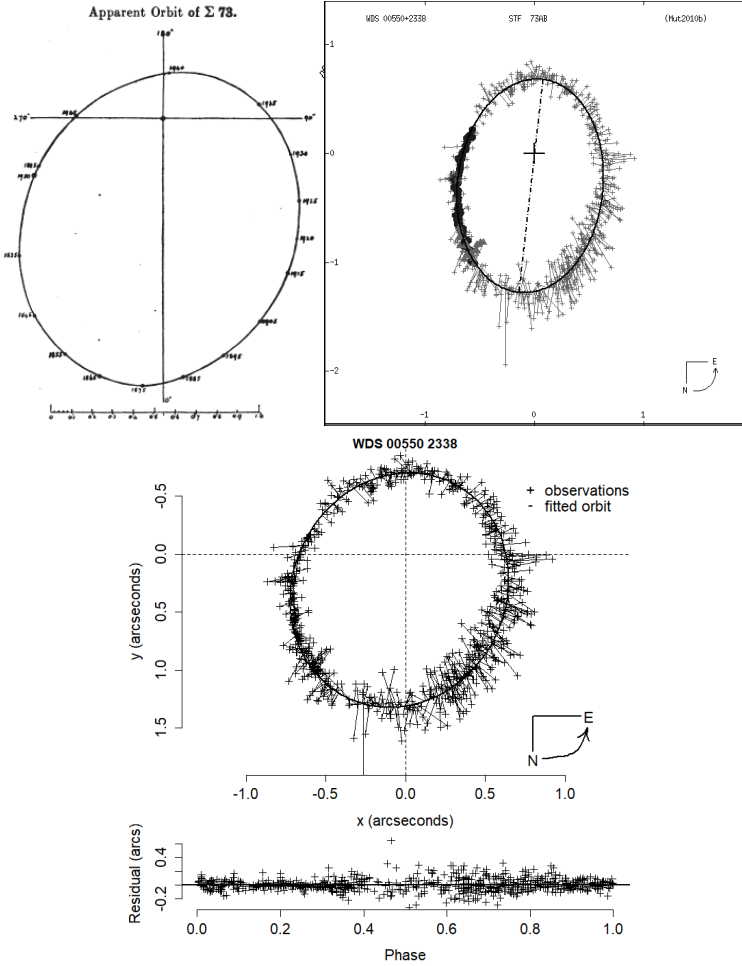
$$\pi_d = \frac{1000a}{P^2(M_1 + M_2)^{\frac{1}{3}}},$$

which is equation 52 in Chapter 14 of Smart<sup>7</sup>, where  $\pi_d$  is in milliarcseconds,  $a$  is in arcseconds,  $P$  is in Besselian years, and the masses are in solar masses. The masses were estimated from the spectral classes of the two stars when they were available in the literature. If only the spectral class of one star was known, then  $M_1 + M_2$  was replaced with 2.0 solar masses in accordance with Smart<sup>7</sup>.

	$P$	$a$	$M_1 + M_2$	$M$ ( $2M_\odot$ )	$\pi_d$	$\pi(H)$	$\pi(G)$
D-1	124.2	0.970	2.10		30.43	26.33	23.31
W	167.4	0.984	2.10		25.30	26.33	23.31
F	168.6	1.014	2.10		25.95	26.33	23.31
D-2	167.4	0.974	3.01		22.21	25.26	24.00
W	145.4	0.890	3.01		22.29	25.26	24.00
F	145.0	0.844	3.01		1.18	25.26	24.00
D-3	216.9	0.407		2.00	8.95	7.60	5.50
W	522.2	0.625		2.00	7.65	7.60	5.50
F	495.0	0.619		2.00	7.85	7.60	5.50
D-4	95.2	0.440		2.00	16.75	9.85	
W	188.0	0.549		2.00	13.28	9.85	
F	189.0	0.568		2.00	13.69	9.85	
D-5	88.2	0.627		2.00	25.12	24.56	22.67
W	98.0	0.743		2.00	27.74	24.56	22.67
F	94.0	0.751		2.00	28.83	24.56	22.67
D-6	59.6	0.350		2.00	18.21	16.14	
W	58.0	0.343		2.00	18.17	16.14	
F	57.0	0.326		2.00	17.47	16.14	
D-7	110.1	0.319		2.00	11.02	6.41	
W	104.6	0.329		2.00	11.76	6.41	
F	105.0	0.353		2.00	12.59	6.41	
D-8	361.0	1.000	3.24		13.33	11.08	11.81
W	421.0	1.071	3.24		12.89	11.08	11.81
F	486.0	1.130	3.24		12.35	11.08	11.81
D-9	220.4	1.205	3.56		21.63	16.42	17.72
W	245.0	1.111	3.56		18.58	16.42	17.72
F	242.0	1.005	3.56		16.95	16.42	17.72
D-10	193.6	2.549	1.48		66.84	74.58	74.09
W	156.0	2.443	1.48		73.98	74.58	74.09
F	157.0	2.438	1.48		73.51	74.58	74.09

TABLE II (concluded)

	$P$	$a$	$M_1 + M_2$	$M$ ( $2M_\odot$ )	$\pi_d$	$\pi(H)$	$\pi(G)$
D-11	238.0	1.060	2.17		21.32	23.14	22.77
W	253.0	1.111	2.17		21.45	23.14	22.77
F	250.0	1.100	2.17		21.41	23.14	22.77
D-12	88.5	0.330		2.00	13.19	11.93	
W	89.0	0.327		2.00	13.02	11.93	
F	89.0	0.315		2.00	12.54	11.93	
D-13	234.8	1.271	2.80		23.69	28.93	26.58
W	257.0	1.450	2.80		25.45	28.93	26.58
F	261.0	1.466	2.80		25.47	28.93	26.58
D-14	317.5	2.870	1.63		52.40	50.87	51.74
W	229.0	2.231	1.63		50.65	50.87	51.74
F	224.0	2.250	1.63		51.83	50.87	51.74
D-15	110.0	1.328	4.52		34.99	18.84	
W	129.0	0.898	4.52		21.27	18.84	
F	129.0	0.951	4.52		22.53	18.84	
D-16	126.1	0.935		2.00	29.51	37.00	
W	120.0	0.975		2.00	31.81	37.00	
F	122.0	0.956		2.00	30.85	37.00	
D-17	154.5	0.783	2.51		20.01	17.12	15.74
W	274.0	1.039	2.51		18.12	17.12	15.74
F	267.0	1.013	2.51		17.98	17.12	15.74
D-18							
W	88.0	0.278		2.00	11.15	11.58	
F	87.0	0.265		2.00	10.71	11.58	
D-19	423.5	1.330		2.00	18.72	18.25	
W	294.0	1.190		2.00	21.36	18.25	
F	288.0	1.151		2.00	20.95	18.25	
D-20	354.9	1.205		2.00	19.08	15.50	16.32
W	510.0	1.424		2.00	17.71	15.50	16.32
F	514.0	1.420		2.00	17.56	15.50	16.32
D-21	321.0	2.120	4.37		27.66	19.77	21.15
W	657.0	2.689	4.37		21.76	19.77	21.15
F	626.0	2.540	4.37		21.23	19.77	21.15
D-22	128.0	0.566	2.73		15.94	15.70	
W	178.0	0.688	2.73		15.56	15.70	
F	163.0	0.635	2.73		15.23	15.70	
D-23	151.7	0.695	2.56		17.86	16.47	16.51
W	201.0	0.816	2.56		17.38	16.47	16.51
F	199.0	0.834	2.56		17.89	16.47	16.51
D-24	85.7	0.790	1.66		34.32	31.20	30.55
W	97.0	0.743	1.66		29.72	31.20	30.55
F	96.0	0.722	1.66		29.08	31.20	30.55
D-25	40.8	0.500	1.81		34.62	20.15	20.03
W	217.0	0.879	1.81		19.97	20.15	20.03
F	264.0	0.885	1.81		17.65	20.15	20.03



FIGS. 1, 2, AND 3

Orbital plots of WDS 00550+2338 from Dyson (1), WDS (2), and FITASTROMETRY (3) for comparison. The lower panel shows the residuals for the orbit immediately above it.

This highlights the potential problem that an ambiguity in the optimized solution can arise if the data set covers only a fraction of the total orbital period and/or if there is an appreciable scatter in the data set. Two other binary systems (2 and 17) exhibited the same difficulty. The optimized solutions of these other two systems are also found in the on-line appendix at: <https://michaelrhodesbyu.weebly.com>.

TABLE III

Results of the astrometric fittings of WDS 00550+2338. The three methods are Dyson (D), WDS (W), and FITASTROMETRY (F).  $P$  is in years,  $a$  in arcseconds,  $\omega$ ,  $i$ , and  $\Omega$  are in degrees, and  $T_0$  is in decimal tropical years AD.  $\chi^2/n$  is the normalized  $\chi^2$  goodness of fit measure, where  $n$  is the number of observations.  $\Delta l$  is the recalculated error estimate, where the initial error estimate is multiplied by the term  $\sqrt{\chi^2/n}$ .

	$P$	$a$	$e$	$\omega$	$i$	$\Omega$	$T_0$	$\chi^2$	$\chi^2/n$	$\Delta l$
D	124.20	0.97	0.708	76.5	41.2	105.7	1815.93			
W	167.510	0.9837	0.306	358.62	44.57	173.66	1956.2			
F	168.6 ± 0.3	1.014 ± 0.003	0.308 ± 0.002	358.6 ± 0.6	45.2 ± 0.3	173.8 ± 0.4	1956.3 ± 0.2	2695	3.7	0.1

TABLE IV

Statistical coefficients of determination ( $R^2$ ) for all 25 Dyson binary systems by fitted parameter comparing the WDS values to those derived by FITASTROMETRY, WDS to Dyson, and then WDS to adjusted Dyson in turn.  $P$  is in years,  $a$  in arcseconds,  $\omega$ ,  $i$ , and  $\Omega$  are in degrees.

Parameter	WDS to FITASTROMETRY	WDS to Dyson	WDS to adjusted Dyson	Linear regression gradient (WDS to FITASTROMETRY)
$\omega$	0.99	0.07	0.76	0.971 ± 0.021
$i$	0.99	0.00	0.53	1.102 ± 0.022
$\Omega$	0.92	0.50	0.51	0.945 ± 0.059
$P$	0.98	0.85	0.85	0.991 ± 0.025
$a$	0.99	0.95	0.84	0.987 ± 0.006
$e$	0.99	0.50	0.50	1.022 ± 0.014

TABLE V

Fitting results for the WDS (W) and FITASTROMETRY (F) methods for the system WDS 00550+2338, where the initial parameter values  $P$ ,  $a$ ,  $e$ ,  $\omega$ ,  $i$ ,  $\Omega$ , and  $T_0$  were taken from the Dyson (D) fit. The Dyson parameter values are given for easy reference.  $P$  is in years.  $a$  is in arcseconds.  $\omega$ ,  $i$ , and  $\Omega$  are in degrees.  $T_0$  is in decimal tropical years AD.

	$P$	$a$	$e$	$\omega$	$i$	$\Omega$	$T_0$	$\chi^2$	$\chi^2/n$	$\Delta l$
D	124.20	0.97	0.708	76.5	41.2	105.7	1815.93			
W	167.510	0.9837	0.306	358.62	44.57	173.66	1956.2	1574		
F	116 ± 8	1.0 ± 0.2	0.75 ± 0.09	73 ± 9	43 ± 13	106 ± 10	1817 ± 5	83	3.0	0.09

TABLE VI

Fitting results for the FITASTROMETRY (F) method for the system WDS 00550+2338, where the initial parameter values  $P$ ,  $a$ ,  $e$ ,  $\omega$ ,  $i$ ,  $\Omega$ , and  $T_0$  were taken from the WDS (W) fit. Units and measures are the same as in Table V. The WDS and Dyson (D) optimal parameter values are given for reference.

	$P$	$a$	$e$	$\omega$	$i$	$\Omega$	$T_0$	$\chi^2$	$\chi^2/n$	$\Delta l$
D	124.20	0.97	0.708	76.5	41.2	105.7	1815.93			
W	167.510	0.9837	0.306	358.62	44.57	173.66	1956.2			
F	170 ± 60	1.0 ± 0.3	0.3 ± 0.3	358 ± 9	46 ± 16	172 ± 10	1954 ± 20	89	3.0	0.1

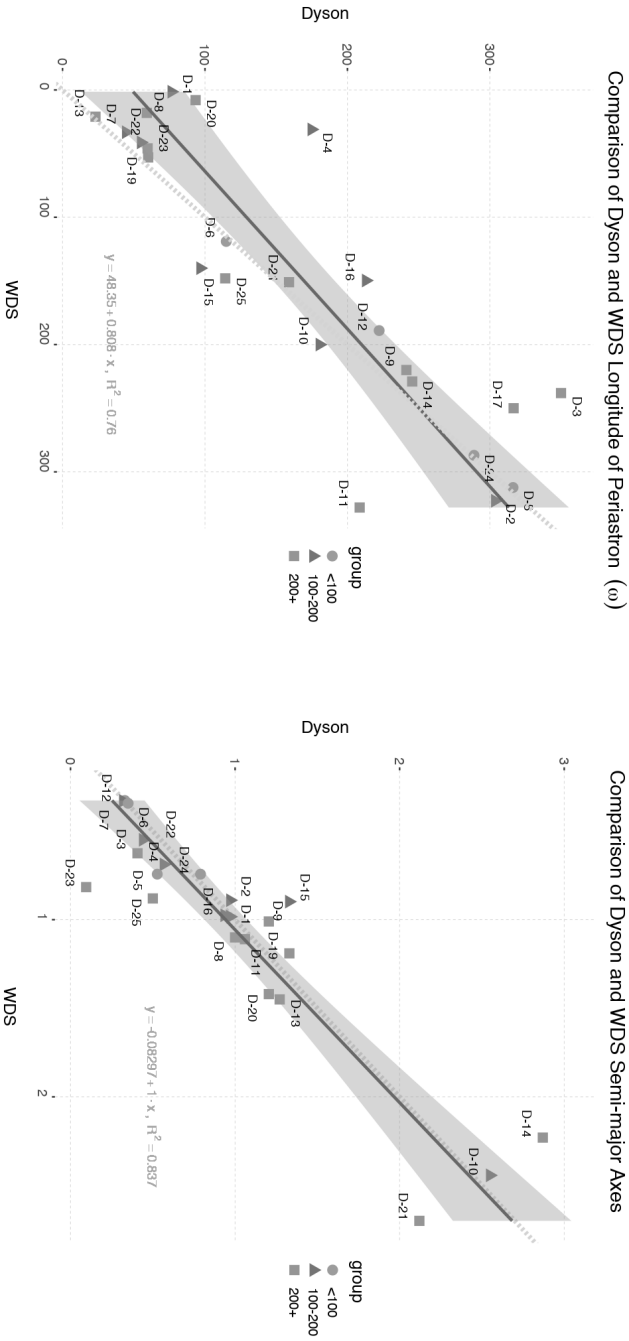


FIG. 4

The left-hand chart is a comparison of the longitude of periastron ( $\omega$ , in degrees) estimates of the Dyson solutions *versus* those of WDS, while the right-hand chart compares the Dyson semi-major axis estimates ( $a$ , arcseconds) against those from WDS. The WDS solution used all available data to the current day. Systems have been classed into three groups based on their WDS periods.

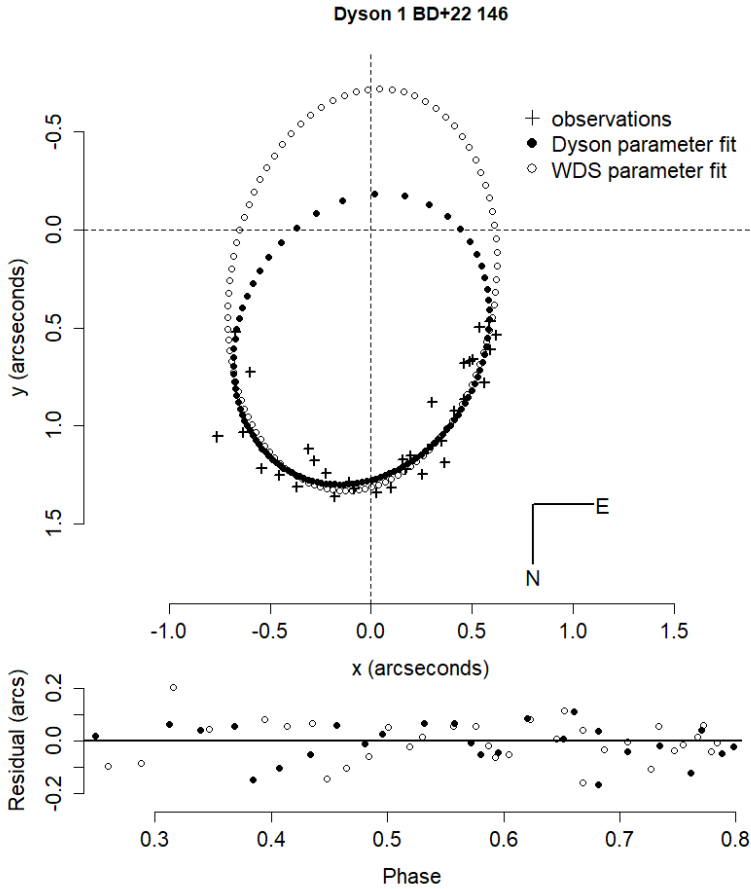


FIG. 5

Plots of FITASTROMETRY model apparent orbits of WDS 00550+2338 (BD+22 146, 36 And) comparing the curve obtained using Dyson or WDS values of the orbital parameters as starting values.

### Conclusions

The main findings from our analysis of the 25 datasets in Dyson's (1921) catalogue can be summarized as follows:

(i) There is a good general agreement between the parameters of WDS and FITASTROMETRY when applied to the fuller WDS datasets, confirming that FITASTROMETRY's optimization algorithm performs satisfactorily where the prior parameters are not far from optimal. Such agreement has given us confidence to apply FITASTROMETRY to the previously unmodelled system V410 Pup<sup>18</sup>, and to make this facility part of our 'analysis toolkit' for future systems.

(ii) The degree of agreement between the results of Dyson and later findings reflects the quantity and quality of available data. In this connection, the issue of local minima in the  $(\chi^2, \alpha)$  hyperspace manifests itself, giving rise to alternative best-fit parameters, particularly with incomplete coverage or scattered data.

(iii) If the data set only covers a fraction of the complete orbit or there is significant scatter, FITASTROMETRY can often find at least two good model fits, depending on the choice of priors. This does not occur if the dataset covers a complete orbit and, as expected with more recent data, the scatter is low.

(iv) The analysis of 36 And, concentrated on in this presentation, allows a few general inferences. Thus, we found from fitting the Dyson datasets that, starting from their adopted priors in either case, both the Dyson and WDS posterior parameters were compatible, although the latter have large uncertainties and approach a ‘long valley’ with a noticeable  $\omega$ – $\Omega$  correlation. In fact, the sum  $\omega + \Omega \approx 170^\circ$  is about the same for either result. This can be understood, as for small  $i$  the two angles merge into one — the position angle of the major axis of a near face-on orbit. The large error estimates of the WDS posteriors at the cessation of iterations are associated with a decline in convexity of the  $(\chi^2, \alpha)$  hypersurface. Numerical procedures become less accurate as the divisors become small, while the value of  $\chi^2$  hardly changes through many iterations. Although the angular parameters from the two fittings are markedly different, there is better consistency in the mass-related quantities, particularly  $a$ , the semi-major axis in arcseconds (Table III).

#### Acknowledgements

This research has made use of the *Washington Double Star Catalogue* maintained at the U.S. Naval Observatory. We thank Prof. Talar Yontan for discussion on *Gaia* and *Hipparcos* measurements.

#### References

- (1) F. W. Dyson, *Catalogue of Double Stars* (H.M. Stationery Office, London), 1921.
- (2) W. Herschel, *Phil. Trans. Royal Soc.*, **93**, 339, 1803.
- (3) N. Shatsky & A. Tokovinin, *A&A*, **382**, 92, 2002.
- (4) S. Söderhjelm, *A&A*, **341**, 121, 1999.
- (5) M. A. Al-Wardat et al., *PAS:A*, **38**, 2002.
- (6) DR3, *A&A*, **674**, A1, 2023.
- (7) W. M. Smart, *Textbook on Spherical Astronomy, 6th Edition* (Cambridge University Press), 1977.
- (8) I. Ribas, F. Arenou & E. F. Guinan, *AJ*, **123**, 2002.
- (9) I. J. D. Craig & J. C. Brown, *Inverse Problems in Astronomy, A guide to inversion strategies for remotely sensed data* (CRC Press), 1986.
- (10) E. Budding & O. Demircan, *A Guide to Close Binary Systems* (CRC Press), 2022.
- (11) W. H. Press et al., *Numerical Recipes: The Art of Scientific Computing* (Cambridge University Press) 1986, p. 523.
- (12) P. R. Adby & M. A. Dempster, *Introduction to Optimization Methods*, (Chapman and Hall Limited) 1974, p. 204.
- (13) P. R. Bevington, *Data reduction and error analysis for the physical sciences* (McGraw-Hill), 1969, p. 228.
- (14) E. Budding & O. Demircan, *loc. cit.*, 2022, ch. 5.
- (15) J. Jackson, *MNRAS*, **80**, 543, 1920.
- (16) B. D. Mason, G. L. Wycoff & W. I. Hartkopf, *The Washington Double Star Catalogue*, 2022.
- (17) M. A. C. Perryman et al., *The Hipparcos Catalogue, A&A*, **323**, L49, 1997.
- (18) A. Erdem et al., *MNRAS*, **515**, 6151, 2022.

THE PERIOD BEHAVIOUR OF THE W URSAE MAJORIS SYSTEMS  
V530 ANDROMEDAE AND V719 HERCULIS

By Christopher Lloyd

*School of Mathematical and Physical Sciences, University of Sussex*

V530 And and V719 Her are W UMa stars with two of the most extreme rates of period change, but in both cases these have been discounted. Contrary to previous results V530 And shows a small positive period change amounting to  $\dot{P} = +0.010(1) \text{ s yr}^{-1}$ , which is about an order of magnitude lower than the dispersion seen in W UMa systems. V719 Her on the other hand, in addition to being a very active system, shows a complex pattern of period behaviour with two period reversals of  $\Delta P/P = \pm 1 \times 10^{-5}$  through a series of discrete period changes between largely constant-period sections.

*Introduction*

Period changes are observed in the majority of W Ursae Majoris systems and can be attributed to light-travel-time effects due to the action of third or more bodies and/or changes due either to period reversals or apparently secular variations. Magnetic fields have a large effect on the light-curves through chromospheric activity in cooler systems, but their influence as an agent of long-term change is not clear. For systems that apparently show continuous secular changes the number showing positive or negative period changes is approximately equal with mean  $\dot{P}$  being effectively zero with a standard deviation of  $0.17 \text{ s yr}^{-1}$  from Latković *et al.*'s<sup>1</sup> sample of individual systems, and  $\sim 10^{-6} \text{ d yr}^{-1} = 0.09 \text{ s yr}^{-1}$  from Kubiak *et al.*'s OGLE sample<sup>2</sup>. The two stars discussed here have the largest negative rate of period change in Latković *et al.*'s sample at  $\dot{P} = -1.53 \text{ s yr}^{-1}$  and  $\dot{P} = -0.53 \text{ s yr}^{-1}$ , well outside the usual dispersion.

*V530 Andromedae*

V530 And is a sparsely observed, long-period,  $P = 0^d.5772$ , W Ursae Majoris system, with  $V = 12.45$  at maximum and eclipses  $0^m.6$  and  $0^m.4$  deep. The eclipses are total and it also shows a weak, positive O'Connell effect of  $\sim 0^m.01$ . The system is in marginal contact, with  $q = 0.386^{3,4}$ . The 2MASS-derived temperature  $T_{\text{eff}} = 6750 \text{ K}$  and period place the system on the boundary of the early/late-type populations of Jayasinghe *et al.*<sup>5</sup>. In a sample of 700 W UMa systems compiled by Latković *et al.*<sup>1</sup> it is listed as the system with by far the largest absolute rate of period change, with  $\dot{P} = -1.53 \pm 0.02 \text{ s yr}^{-1}$ , which is twice the size of the next-largest system. The value of  $\dot{P}$  comes from period, and wider photometric, studies by Samec *et al.*<sup>3,4</sup>, which for brevity will be later referred to as S13 and S16, respectively.

The variability of V530 And was discovered by Khruslov<sup>6</sup> in data from the Northern Sky Variability Survey (NSVS, Woźniak *et al.*<sup>7</sup>) which are no longer publicly available. Khruslov referred to the star as NSVS 6447718 and provided an ephemeris of primary minimum

$$H\tilde{J}D_{\text{Minl}} = 2451479.632 + 0.57723 \times E, \quad (1)$$

together with a light-curve showing the clear and unambiguous difference between the minima. The ephemeris is of relatively low precision as the *NSVS* data cover only the second half of 1999. Fitting a 6-harmonic Fourier function to the *NSVS* data with errors  $< 0^m.06$  gives an ephemeris of primary minimum of

$$H\tilde{J}D_{\text{Minl}} = 2451479.6354(8) + 0.577234(33) \times E, \quad (2)$$

which is consistent with Khruslov's and provides a measure of the uncertainties. Two further minima were measured by S13<sup>3</sup> in 2011, and to calculate their updated ephemeris they took nine individual faint points from the *NSVS* data and also used Khruslov's composite timing. In their second paper, S16<sup>4</sup>, they used a revised set of eight *NSVS*-derived timings and four new timings from observations made between 2013 October and 2014 January. In combination with their earlier data they constructed a quadratic ephemeris giving the large negative period change that has entered the literature.

There are very few other independent timings of V530 And. The O-C Gateway (OCG)\* lists just nine, including Khruslov's original measurement. However, these timings together with the four from S16 provide a precise linear ephemeris of primary minimum

$$H\tilde{J}D_{\text{Minl}} = 2451479.6316(8) + 0.57723954(8) \times E, \quad (3)$$

that is entirely consistent with Khruslov's original ephemeris, has an r.m.s. residual of  $0^d.0015$ , and does not require any period change. The only points that are inconsistent with this ephemeris are the two minima from S13<sup>3</sup> and the additional *NSVS*-derived timings they used.

The problem with the *NSVS*-derived timings is clear in their O-C diagram (see Fig. 3 of S13<sup>3</sup>), where there is a systematic difference of  $\sim 0^d.06$  between their *NSVS* timings and Khruslov's ephemeris. The reason is due to the half-day difference between JD and MJD, which is how the *NSVS* times are reported. For reasons that are not clear, all these timings, including Khruslov's time of primary minimum, are assigned as secondary minima. In their second paper Khruslov's timing is omitted and a modified set of *NSVS*-derived timings is used, but of the three that appear in the first set, all have their previous eclipse assignments changed.

The inconsistency of the two timings given by S13<sup>3</sup> comes down to a one-day error in the date. According to their paper the data were taken on 2011 September 27 and 29. However, the observations as listed in their table 1 were made during JD 245530.6–31.0 and 32.8–33.0, which correspond to 2011 September 26.1–26.5 and September 28.3–28.5. Sample FITS headers from two of these observations confirms that the HJDs as tabulated are for some unknown reason one day early (Samec, private communication). Adding one day to their timings removes this discrepancy and leads to a linear ephemeris consistent with Equation 3 with an r.m.s. residual of  $0^d.0016$ .

In an effort to increase the number of timings, additional data are taken from *Catalina Sky Survey* (CSS<sup>8</sup>), the *All-Sky Automated Survey for Supernovae* (ASAS-SN) archives<sup>9,10</sup>, and the *Asteroid Terrestrial-Impact Last Alert System* (ATLAS) project<sup>11,12</sup>. As with the *NSVS* data the times of minima have been calculated by using a 4- or 6-harmonic Fourier fit depending on the quality of

\*O-C Gateway: <http://var2.astro.cz/ocgate/index.php>

the data. The *CSS* data are taken in the *V* band and cover the years 2005–2013, but the light-curve is relatively poorly defined so they have not been divided into shorter sets, and just the one primary and secondary timing are measured for the whole interval. The *ASAS-SN* data cover the years 2012–2019 in *V* and 2016–2023 in Sloan *g*. These are divided into mostly annual sets with the poorer coverage in the early years being combined as necessary, and similarly with the *ATLAS* data which cover the years 2016–2023 in their cyan (*c*) and orange (*o*) bands. The *c* data are relatively sparse and these are combined into multi-year sets.

The system has also been observed by the *Transiting Exoplanet Survey Satellite* (*TESS*)<sup>13</sup> during 2019 November in Sector 17 at the standard 30-minute cadence, and during 2022 November in Sector 57 with a much higher cadence of 200 seconds. The data were extracted from the Full-Frame Images using the *LIGHTKURVE* package<sup>14</sup> and restricted to *HARD* quality in *LIGHTKURVE* parlance. The fluxes were measured using a slight variant of the default aperture created within the routine due to the high background and the possible contamination by two nearby stars. To help minimize this the sky background was measured in a one-pixel-wide frame, around the aperture, and this was subtracted from the target flux. The sky-subtracted flux shows the full amplitude of the light-curve and is also better corrected in the high-noise sections of data. The resulting light-curve is relatively smooth but some discordant sections were removed and additional flattening with a low-order polynomial fitting was required to correct variation in level through the *TESS* orbit, as is often the case. The *TESS* sectors naturally divide into two due to the 1–2 day break for the data downlink, so the light-curve comprises four sections of  $\sim 11$  days of mostly continuous data. The phase diagram shown in Fig. 1 is derived from an 8-harmonic Fourier fit. There is little systematic deviation from the mean light-curve and the residuals have an r.m.s. error of  $0^{\text{m}}.0075$ . The amplitudes of primary and secondary eclipses are  $0^{\text{m}}.62$  and  $0^{\text{m}}.39$  — marginally smaller than the ground-based data — and the maxima show a small O’Connell effect of  $0^{\text{m}}.01$ . Timings were calculated for every two cycles using a fixed-frequency Fourier fit and these reveal a small

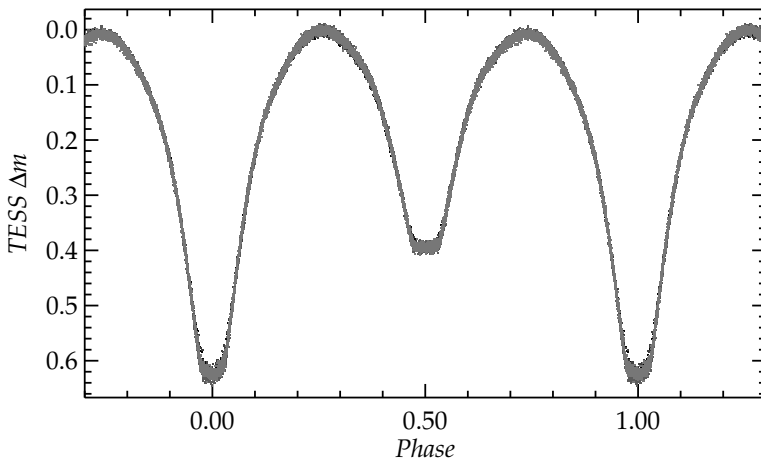


FIG. 1

The phase diagram of the *TESS* data for V530 And folded on the best-fit period derived from an 8-harmonic Fourier fit. The different half-sectors are shown in different greyscales.

TABLE I

Sample table — Times of minimum of *V*530 And from 2000 onwards

HJD	$\sigma$ (d)	Min.	Cycle	O-C (d)	Band	Data set
2451431.7243	0.0012	1	-8896.0	0.0035	R	NSVS (This paper)
2451432.0123	0.0015	2	-8895.5	0.0029	R	NSVS (This paper)
2451479.632	—	1	-8813.0	0.0003	R	NSVS Khruslov <sup>6</sup>
2451514.8466	0.0014	1	-8752.0	0.0033	R	NSVS (This paper)
2451515.1358	0.0019	2	-8751.5	0.0039	R	NSVS (This paper)
2454928.0602	0.0017	1	-2839.0	-0.0009	V	CSS (This paper)
2454928.3515	0.0035	2	-2838.5	0.0018	V	CSS (This paper)
2455831.72806	0.00045	2	-1273.5	-0.0017	UBV RI	S13 <sup>3</sup>
2455833.74595	0.00040	1	-1270.0	-0.0041	UBV RI	S13 <sup>3</sup>
2456488.33546	0.00102	1	-136.0	-0.0043	V	ASAS-SN (This paper)

This table is available at CDS by anonymous ftp to cdsarc.u-strasbg.fr (130.79.128.5) or via <https://cdsarc.unistra.fr/viz-bin/cat/J/other/Obs/I44.I4>

but consistent offset between the primary and secondary minima of  $0^d.0005$  for Sector 17 and  $0^d.001$  for Sector 57, with the secondary minima being slightly later. These differences probably reflect small and slow changes in the distribution of the spots found by Samec *et al.* The mean times for both minima (strictly BJD) were measured for each of the half-sectors and these are collected with all the other times of minimum in Table I, a small sample of which is given here. The difference between BJD and HJD is a few seconds and insignificant in this context.

The O-C diagram is shown in Fig. 2 and despite the large gap between the NSVS and CSS data it is obvious that there is no large period change; in fact for W UMa systems the range of variation is very modest, but it is nevertheless clear that a small, apparently secular change has occurred. The unweighted

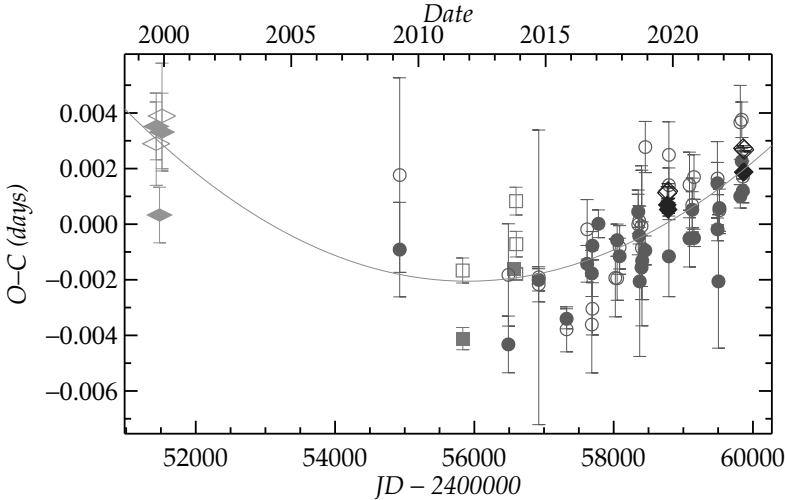


FIG. 2

The O-C diagram of *V*530 And showing two pairs of timings derived from NSVS data (lozenges) with Khruslov's  $T_0$ , the corrected S13 timings as described in the text and S16 timings (squares), the TESS data (diamonds), the OCG data and other new timings (circles) as given in Table I. Open symbols show the secondary minima. The line shows the best unweighted quadratic fit to the data as given in Equation 4.

quadratic fit to the data gives an ephemeris of primary minimum of

$$HJD_{\text{MinI}} = 2456566.84244(27) + 0.577239807(47) \times E + 8.52(88) \times 10^{-11} \times E^2, \quad (4)$$

leading to a small positive period change of  $\dot{P} = +0.010(1) \text{ s yr}^{-1}$  that is at least an order of magnitude smaller than the dispersion found in the surveys. The data cover such a short time-span and the range of the residuals is so small that it is impossible to put any constraints on the nature of the period behaviour, but any cyclical changes would require a period in excess of 30 years.

### V719 *Herculis*

V719 Her is also a relatively recent discovery but it is a star with something of a chequered history. It was identified as a likely RRab variable by Kurochkin<sup>15</sup> with  $P = 0^d.33587$ , but notes in the *GCVS* suggest that it was also considered as a *W UMa* system with twice that period. The situation was resolved by Schmidt<sup>16</sup> who found it was a *W UMa* system with  $P = 0^d.400995$ , which is the 1-day alias of the original period. The star has  $V = 12.3$  at maximum with eclipses  $0^m.55$  and  $0^m.35$  deep. The only photometric model of the system is provided by Goderya *et al.*<sup>17</sup> who find the system has  $q = 0.296$ , which is near the median for *W UMa* systems, but give a rather large value for the fillout factor,  $f = 46\%$ . They assume  $T_1 = 6580 \text{ K}$  and derive  $T_2 = 6267 \text{ K}$ , but the modern *Gaia*-derived mean value for the system is significantly cooler at  $T_{\text{eff}} = 5680 \text{ K}$ , placing the star well into the cool population of Jayasinghe *et al.*<sup>5</sup>. Goderya *et al.* also made a rather limited period study of the system based on their new data and Schmidt's earlier timing, and found a very significant period decrease amounting to  $\dot{P} = -0.54 \text{ s yr}^{-1}$ . Unfortunately, Schmidt's timing referred to maximum light as the star had originally been considered as a pulsator. Further observations by Schmidt<sup>18</sup> revealed significant variation in the shape of the light-curve and in particular the depths of the eclipses, and also showed that the new timings were not consistent with the quadratic ephemeris. All these timings have been redetermined here. Since then approximately 50 independent eclipse timings have been published and are collected by the O-C Gateway.

New minima have been calculated from the synoptic surveys *NSVS*, *CSS*, *ASAS-SN*, *ATLAS*, as above, and in this case also the *Zwicky Transient Facility (ZTF)*<sup>19</sup>, which provides good coverage from 2017 to date in the Sloan *zg* and *zr* variants. Near the maximum some of the *zr* data show saturation effects but the minima are unaffected. Timings have also been taken from the *TESS* data but these will be discussed in more detail later. The times of minima for V719 Her are listed in Table II; again a small sample is given here.

The period behaviour of V719 Her has also been investigated prior to discovery using the Harvard photographic data, which have been taken from the Digital Access to a Sky Century at Harvard (DASCH) archive\*. The data are very inhomogeneous with a relatively sparse set taken between about 1890–1930 (JD 2411000–2427000), with a much more dense set taken between about 1930–1950 (JD 2427000–2434000). A similar set of observations covers the interval from 1965–1990 (JD 2439000–2448000). When restricted to observations with errors  $< 0^m.2$  these data sets contain 129, 429, and 405 data points, respectively. None of the Harvard data are contemporaneous with any other published observations.

\*DASCH <https://library.cfa.harvard.edu/search-dasch>

TABLE II

Sample table — Times of minimum of V719 Her from 1905 onwards

HJD	$\sigma$ (d)	Min.	Cycle	O-C (d)	Band	Data set
2416588.4291	0.0044	1	-94602.0	0.0255	pg	Harvard (This paper)
2416588.6370	0.0049	2	-94601.5	0.0329	pg	Harvard (This paper)
2422894.5583	0.0052	1	-78873.0	0.0419	pg	Harvard (This paper)
2422894.7650	0.0061	2	-78872.5	0.0356	pg	Harvard (This paper)
2428985.8523	0.0034	1	-63680.0	0.0470	pg	Harvard (This paper)
2428986.0556	0.0037	2	-63679.5	-0.0441	pg	Harvard (This paper)
2432297.9125	0.0037	1	-55419.0	0.0530	pg	Harvard (This paper)
2432298.1108	0.0038	2	-55418.5	0.0552	pg	Harvard (This paper)
2442573.7768	0.0044	1	-29789.0	-0.0267	pg	Harvard (This paper)
2442573.9709	0.0047	2	-29788.5	0.0203	pg	Harvard (This paper)

This table is available at CDS by anonymous ftp to [cdsarc.u-strasbg.fr](https://cdsarc.u-strasbg.fr) (130.79.128.5) or via <https://cdsarc.unistra.fr/viz-bin/cat/J/other/Obs/144.14>

To avoid any unexpected surprises a Discrete Fourier Transform (DFT) periodogram was applied to each section to identify the dominant periods. The first set clearly showed an unambiguous peak at the anticipated half-period of the binary, but the periodogram was relatively noisy. For the other two sets a clear peak appeared at the expected frequency and in addition these DFTs show noticeable aliases at  $f \pm 0.00274 \text{ d}^{-1}$ , corresponding to a spacing of one year. The linear ephemeris was determined from the least-squares 2-harmonic Fourier fit and these are listed in Table III. Each set was divided in two and each half was fitted in the same way to determine composite times of minimum for these segments of the data. A range of initial periods were fitted and these converged to give unambiguous periods for each section. Despite the faintness of the photographic light-curves the primary minima were correctly identified in each case. Due to the sparseness of the first set an additional test was performed to estimate the reliability of the results. The set was divided in two by taking alternate points and the best fit ephemeris derived as before for each subset, and were found to be consistent.

The full O-C diagram of V719 Her is shown in Fig. 3. The photographic data cover the period from 1890–1990 and the modern data follow on directly. Although the range of the O-C residuals is relatively small there is a clear variation of period following a broadly sinusoidal period reversal. The current period is sensibly identical to the period from the early photographic data, and although it is not directly observed, the period reversal between JD 2435000 and 2440000 ( $\sim 1955$ ) is constrained to a period with a similar difference from the mean by the two shorter sections of photographic data, leading to an overall period change of  $\Delta P/P \sim 1 \times 10^{-5}$ . The period behaviour is not sinusoidal and from the detail of the recent variation shown in Fig. 4 it is more likely that there

TABLE III

Ephemerides for subsets of the data for V719 Her

Data	$T_0$	Period	Range
Harvard (Early)	2420268.910(3)	0.400924(11)	2411000 < JD < 2427000
Harvard (Middle)	2429851.453(3)	0.400927(10)	2427000 < JD < 2434100
Harvard (Late)	2445105.642(2)	0.400929(9)	2439000 < JD < 2448000
Early modern	2450284.401(2)	0.4009278(6)	2447000 < JD < 2452500
Modern	2452741.3016(4)	0.40092391(3)	2452500 < JD < 2460500
TESS	2459530.1458(3)	0.40092414(8)	2458950 < JD < 2459780

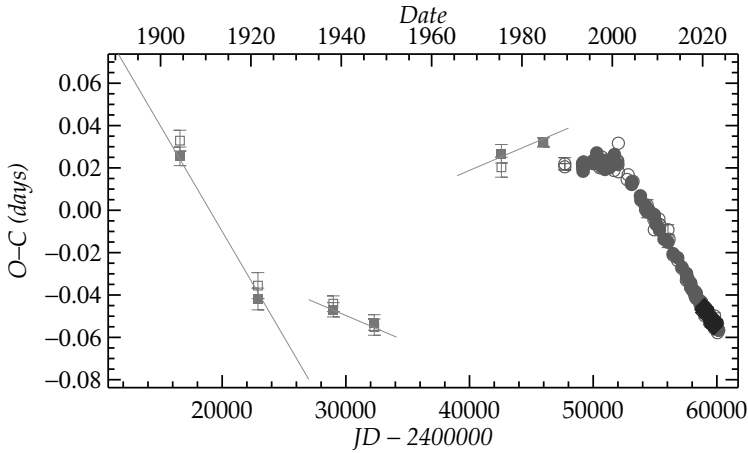


FIG. 3

The full O-C diagram of V719 Her showing the photographic data (squares), other modern data (circles), and *TESS* data (diamonds) constructed using an arbitrary ephemeris. Open symbols indicate secondary minima. The lines show the ephemerides, and extent, of the photographic data, as listed in Table III. The modern data are shown in detail in Fig. 4.

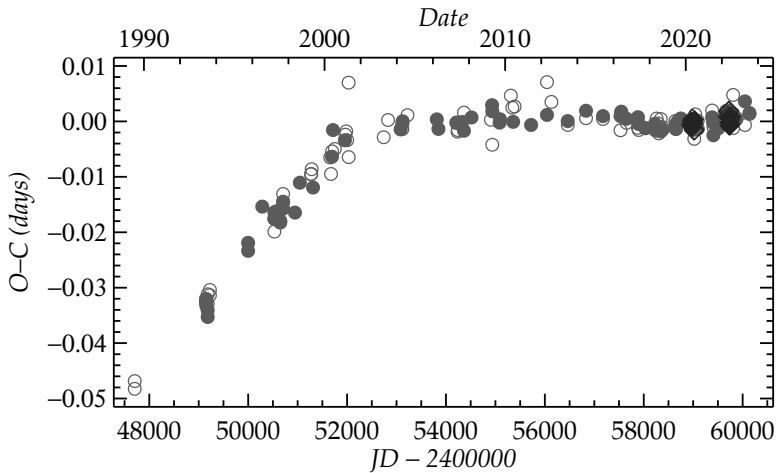


FIG. 4

The O-C diagram of V719 Her relative to the modern ephemeris, showing the modern data with the symbols as before. There is clearly a period change near JD 2452500, and some indication of a small oscillation in the most recent data. The mean periods for these sections are included in Table III.

are discrete changes between constant-period sections. The modern data are shown in detail in Fig. 4 where the most recent period change can be seen near JD 2452500 (2002), but it is also clear that the current period is not strictly constant as there is a slow oscillation, or possible prelude to another change. The behaviour between the late photographic and the early modern data

is not clear as they have very similar periods, but appear to be slightly offset. Although the interpretation in Fig. 3 appears to be the most likely, the gap in the photographic data does allow for an increase in the cycle count. In that scenario the early photographic and modern data are essentially aligned, but the overall dispersion increases to  $0^d.2$ , and to ensure continuity it requires a period change twice that necessary in Fig 3.

V719 Her was observed by *TESS* in Sectors 24, 25, and 26 during 2020 April–June at the standard 30-minute cadence and in Sectors 51, 52, and 53 during 2022 May–June at the 10-minute cadence. The flux used is the standard SAP\_FLUX from the *TESS* Science Processing Operations Center (SPOC) products, as in this case this is the most consistent of the different products that are available. All the data were used apart from two small sections from one sector where the background variation had not been correctly removed, giving 3537 observation for the first set and 10189 for the second. Each of the two sets of three consecutive sectors have approximately 80 days of near continuous data with gaps of 1–2 days between the sectors and half-sectors. The data have been folded on the ephemeris derived from an 8-harmonic Fourier fit,

$$HJD_{\text{MinI}} = 2459530.1458(3) + 0.40092414(8) \times E, \quad (5)$$

and are shown in Fig. 5. The different sectors are shaded differently and show significant variation in the depths of the eclipses and particularly in the relative heights of the maxima, in the classical O’Connell effect<sup>20,21</sup>. Between the two epochs both positive and negative O’Connell effects can be seen and the range of variation is  $\sim 0^m.05$ , and the eclipses show a similar level of variation. The maximum depths are  $0^m.55$  and  $0^m.40$ , very similar to the *R*-band data of Schmidt. Eclipse timings were calculated for every two cycles using a fixed-frequency Fourier fit and these reveal coherent movement of both the primary and secondary eclipse on a time-scale of tens of days. These are shown

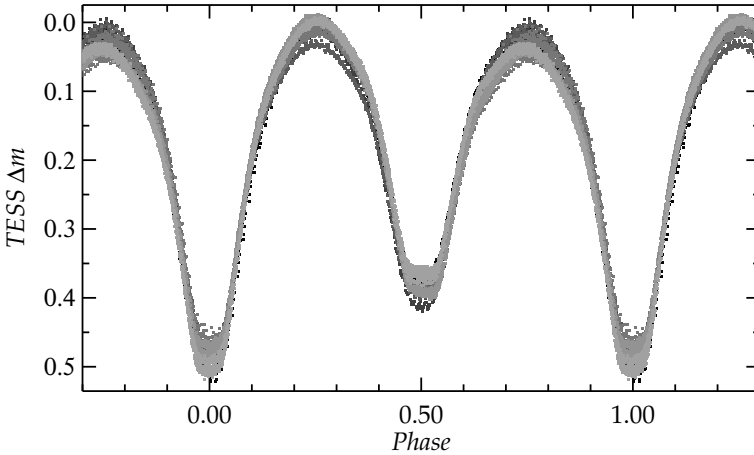


FIG. 5

The phase diagram of V719 Her showing the *TESS* data folded on the best-fit period given in Equation 5. The different sectors are shown in different symbols.

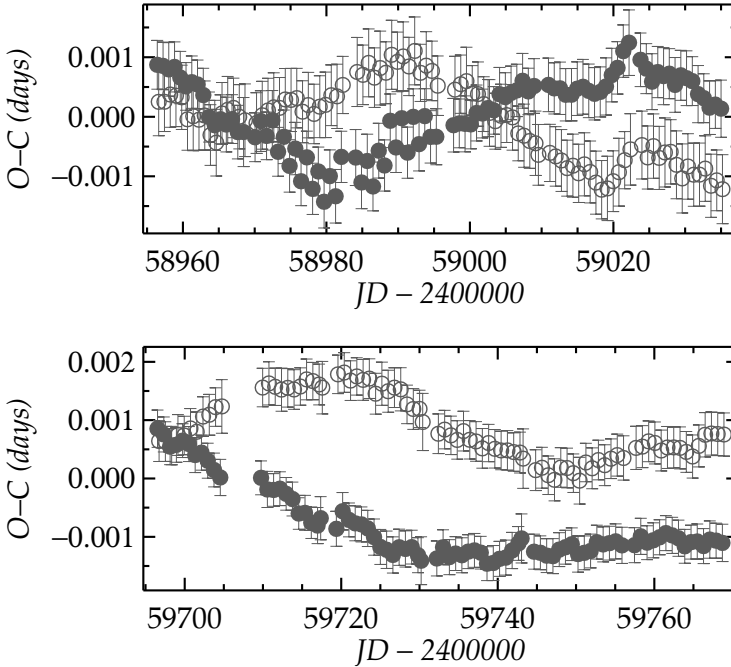


FIG. 6

The O-C diagram of V719 Her showing the timings for every two cycles of the *TESS* data relative to the *TESS* ephemeris. The top panel shows Sectors 24, 25, and 26 and the lower panel Sectors 51, 52, and 53.

for the two sets of data in Fig. 6 where for the first set the movement of the primary and secondary mirror each other, and in the second their movement is more independent. The mean times for both minima were measured for each of the half-sectors and these are collected with all the other times of minimum in Table II and Fig. 3. These variations are most likely due to the movement of spots and again the *TESS* data highlight the speed at which these changes occur. V719 Her will be observed again by *TESS* in Sectors 78–80 (2024 May–July).

### Summary

V530 And and V719 Her were originally selected in order to test the validity of the extreme rates of period change found in the literature but in both cases these have been dismissed. However, a more detailed examination of the systems has led to the discovery of a small positive period change for V530 And amounting to  $\dot{P} = +0.010(1) \text{ s yr}^{-1}$ , which is about an order of magnitude lower than the dispersion seen in *W UMa* systems. V719 Her on the other hand, in addition to being a very active system, shows a complex pattern of period behaviour.

Over the past century the system has undergone two period reversals with  $\Delta P/P = \pm 1 \times 10^{-5}$  through a series of discrete period changes between largely constant-period sections. There is some evidence in the most recent data that there are small oscillations or perturbations, meaning that the linear sections might not be truly constant. Whether this is due to the effect of active regions or a presentation of the wider behaviour is not clear at this time.

#### Acknowledgements

The author is indebted to Ron Samec for providing crucial information about the observations reported in S13. The author also appreciates helpful comments from the referee. The author is pleased to acknowledge use of NASA's Astrophysics Data System Bibliographic Services. This research has made use of the *Simbad* database and the *VizieR* catalogue-access tool, CDS, Strasbourg, France (DOI: 10.26093/cds/vizieer). The author gratefully acknowledges use of the AAVSO Variable Star Index (VSX). This paper includes data collected by the *TESS* mission, which are publicly available from the Mikulski Archive for Space Telescopes (MAST). Funding for the *TESS* mission is provided by NASA's Science Mission directorate.

#### References

- (1) O. Latković, A. Čeki & S. Lazarević, *ApJ Suppl*, **254**, 10, 2021.
- (2) M. Kubiak, A. Udalski & M. K. Szymanski, *Acta Astron.*, **56**, 253, 2006.
- (3) R. G. Samec *et al.*, *ISRN Astronomy and Astrophysics*, **2013**, 201235, 2013.
- (4) R. G. Samec *et al.*, *JAVSO*, **44**, 108, 2016.
- (5) T. Jayasinghe *et al.*, *MNRAS*, **493**, 4045, 2020.
- (6) A. V. Khruslov, *Peremennye Zvezdy Prilozhenie*, **8**, 40, 2008.
- (7) P. R. Woźniak *et al.*, *AJ*, **127**, 2436, 2004.
- (8) A. J. Drake *et al.*, *ApJ*, **696**, 870, 2009.
- (9) B. J. Shappee *et al.*, *ApJ*, **788**, 48, 2014.
- (10) C. S. Kochanek *et al.*, *PASP*, **129**, 104502, 2017.
- (11) J. L. Tonry *et al.*, *PASP*, **130**, 064505, 2018.
- (12) K. W. Smith *et al.*, *PASP*, **132**, 085002, 2020.
- (13) G. R. Ricker *et al.*, *Journal of Astronomical Telescopes, Instruments, and Systems*, **1**, 014003, 2015.
- (14) Lightkurve Collaboration *et al.*, 'Lightkurve: Kepler and TESS time series analysis in Python', Astrophysics Source Code Library, record ascl:1812.013, 2018.
- (15) N. E. Kurochkin, *Peremennye Zvezdy Prilozhenie*, **3**, 201, 1977.
- (16) E. G. Schmidt, *AJ*, **102**, 1766, 1991.
- (17) S. N. Goderya, K. C. Leung & E. G. Schmidt, *Ap&SS*, **243**, 315, 1996.
- (18) E. G. Schmidt, *Information Bulletin on Variable Stars*, **4552**, 1, 1998.
- (19) F. J. Masci *et al.*, *PASP*, **131**, 018003, 2019.
- (20) D. J. K. O'Connell, *Publications of the Riverview College Observatory*, **2**, 85, 1951.
- (21) N. J. Wilsey & M. M. Beaky, *Society for Astronomical Sciences Annual Symposium*, **28**, 107, 2009.

REDISCUSSION OF ECLIPSING BINARIES. PAPER 16:  
THE  $\delta$  SCUTI /  $\gamma$  DORADUS HYBRID PULSATOR GK DRACONIS

By John Southworth

*Astrophysics Group, Keele University*

GK Dra is a detached eclipsing binary system containing two early-F stars, one evolved, in an orbit with a period of 9.974 d and a small eccentricity. Its eclipsing nature was discovered using *Hipparcos* data, and pulsations were found in follow-up ground-based data. Extensive observations have been obtained using the *Transiting Exoplanet Survey Satellite* (*TESS*), and we use these and published spectroscopy to perform a detailed reanalysis of the system. We determine masses of  $1.421 \pm 0.012$  and  $1.775 \pm 0.028 M_{\odot}$ , and radii of  $1.634 \pm 0.011$  and  $2.859 \pm 0.028 R_{\odot}$ . The secondary component is more massive, larger, and slightly cooler than its companion; the eclipses are total. The properties of the system can be matched by theoretical predictions for an age of 1.4 Gyr and a slightly sub-solar metallicity. We measure 15 significant pulsation frequencies in the *TESS* light-curve, of which three are in the frequency domain of  $\gamma$  Doradus pulsations and the remaining 12 are  $\delta$  Scuti pulsations; the system is thus a hybrid pulsator. The strongest pulsation can be definitively assigned to the secondary star as it has been detected in radial velocities of that object. *TESS* will observe GK Dra again for ten consecutive sectors in the near future.

### Introduction

Eclipsing binary star systems contain the only stars for which a direct measurement of their most basic properties (mass and radius) is obtainable. Detached eclipsing binaries (dEBs) are particularly useful because their components have evolved as single stars so can be compared to the predictions of theoretical models of stellar evolution, both to check how well the models perform and to guide their improvement<sup>1-3</sup>.

Another approach to constraining the theoretical descriptions of stars is *via* asteroseismology<sup>4</sup>, which uses the measurement of stellar oscillation frequencies to constrain properties such as their densities, ages, and rotational profiles<sup>5-8</sup>.

A significant fraction of stars are known to show the signatures of both eclipses and pulsations in their light-curves. Many of these identifications are a result of the widespread availability of high-quality light-curves from space-based telescopes<sup>9</sup>. The most common class of pulsations seen in dEBs is the  $\delta$  Scuti type<sup>10-12</sup>, which are short-period pulsations (0.015 to 0.33 d<sup>13,14</sup>) with pressure as the restoring force. A smaller number show  $\gamma$  Doradus pulsations<sup>15,16</sup>, which have longer periods (0.3 d to 4 d<sup>14,17</sup>) and gravity as their restoring force. The  $\delta$  Scuti and  $\gamma$  Dor phenomena can occur simultaneously in late-A and early-F stars, examples of which are labelled as hybrid pulsators<sup>14,18</sup>.

In this work we present an analysis of GK Draconis based on published spectroscopy and new space-based photometry. GK Dra is a dEB known to display  $\delta$  Scuti pulsations. We find that it also shows  $\gamma$  Dor pulsations. For further discussion on the motivation of this series of papers see ref. 19.

### GK Draconis

GK Dra (Table I) is one of the 343 eclipsing binaries discovered using data from the *Hipparcos* satellite<sup>25</sup> and named by Kazarovets *et al.*<sup>26</sup>. Dallaporta *et al.*<sup>27</sup> presented the first ground-based photometry, finding an orbital period of  $P = 9.9742$  d, a modest orbital eccentricity, and pulsations in the secondary component consistent with the  $\delta$  Scuti type. The system has since been included in catalogues of binary systems containing  $\delta$  Scuti components<sup>28,29</sup>.

Griffin & Boffin<sup>30</sup> (hereafter GBo3) published the first radial-velocity (RV) study of GK Dra and V1094 Tau (the latter since analysed in detail by Maxted *et al.*<sup>31</sup>). For GK Dra they obtained 50 RVs of each star. A large scatter in the RVs of the more massive component was found and attributed to the effects of pulsations. A variation of 0.1178-d period was included in the fit to the spectroscopic orbit of the star to account for the pulsation signature. This variation was treated as a Keplerian orbit for convenience, and the fitted eccentricity and velocity amplitudes were  $e = 0.26 \pm 0.06$  and  $2.62 \pm 0.17$  km s<sup>-1</sup>, respectively. The RVs for the less massive star were also found to show an excess scatter indicative of possible pulsations. GBo3 found the spectral types of both components to be significantly earlier than the Go given in the *Henry Draper Catalogue*<sup>21</sup> based on the  $B-V$  colour index and the presence of pulsations in at least one of the stars, preferring F2 III–IV for the more massive star.

Zwitter *et al.*<sup>32</sup> (hereafter ZW03) presented the only full analysis of GK Dra published so far. They based their results on data from the *Hipparcos* satellite plus a set of 35 échelle spectra covering 848–874 nm, specifically chosen to simulate the type of data expected from the *Gaia* mission<sup>33</sup>. The masses and radii thus determined were  $M_A = 1.46 \pm 0.07 M_\odot$ ,  $M_B = 1.81 \pm 0.11 M_\odot$ ,  $R_A = 2.43 \pm 0.04 R_\odot$  and  $R_B = 2.83 \pm 0.05 R_\odot$ . These numbers indicate that both components are significantly evolved. The RVs from ZW03 are not of the same quality as those from GBo3, and the *Hipparcos* photometry is greatly inferior to that now available from *TESS*, so a reanalysis of GK Dra is warranted.

TABLE I  
Basic information on GK Draconis

Property	Value	Reference
Right ascension (J2000)	16 <sup>h</sup> 45 <sup>m</sup> 41 <sup>s</sup> .19	20
Declination (J2000)	+68°15'30".9	20
Henry Draper designation	HD 152088	21
<i>Gaia</i> DR3 designation	1648575062872337792	20
<i>Gaia</i> DR3 parallax	3.2954 ± 0.0133 mas	20
<i>TESS</i> Input Catalog designation	TIC 230128667	22
$B$ magnitude	9.12 ± 0.02	23
$V$ magnitude	8.77 ± 0.01	23
$j$ magnitude	8.001 ± 0.023	24
$H$ magnitude	7.886 ± 0.021	24
$K_s$ magnitude	7.864 ± 0.024	24
Spectral type	F1 V + F2 IV	This work

### Photometric observations

GK Dra has been observed extensively by the NASA *Transiting Exoplanet Survey Satellite*<sup>34</sup> (*TESS*) as it lies in the northern continuous viewing zone of that telescope. Data from sectors 14 to 26 (2019/07/18 to 2020/07/04) were obtained at a cadence of 1800 s, although those from sectors 15 and 16 were not available from the archive at the time of writing. Sectors 40 and 41 (2021/06/08 to 2021/08/20), and 47 to 55 (2021/12/30 to 2022/09/01) yield data at a cadence of 600 s. Finally, in sectors 56 to 60 (2022/09/01 to 2023/01/18) GK Dra was observed at a 200-s cadence.

The data from all the sectors mentioned above were downloaded from the NASA Mikulski Archive for Space Telescopes (MAST\*) using the LIGHTCURVE package<sup>35</sup>. The 'hard' flag was used to reject data labelled as of lower quality. We used the simple aperture photometry (SAP) data<sup>36</sup> for consistency with previous papers in this series. The data were converted to differential magnitude and the median magnitude of each sector was subtracted for convenience.

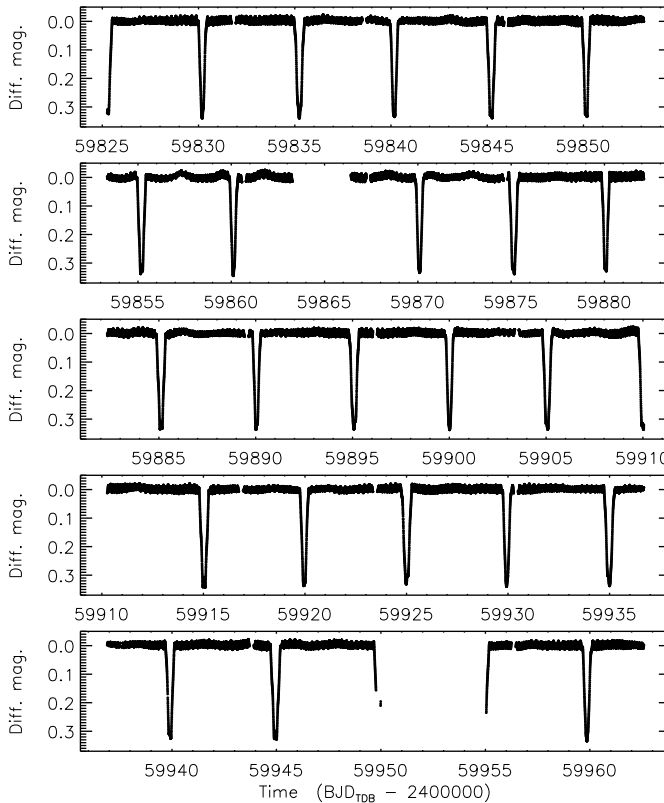


FIG. 1

*TESS* short-cadence SAP photometry of GK Dra. The flux measurements have been converted to magnitude units then rectified to zero magnitude by subtraction of the median.

\*<https://mast.stsci.edu/portal/Mashup/Clients/Mast/Portal.html>

Our results below are primarily based on the 600-s-cadence data as these cover many eclipses whilst avoiding problems with undersampling the light variations of the system. We used the 200-s-cadence data for the pulsation analysis due to its higher frequency resolution. The 200-s data are shown in Fig. 1, where eclipses and pulsations can both be seen. The 600-s data look similar but of course have a lower sampling rate.

We queried the *Gaia* DR3 database\* for objects within 2 arcmin of GK Dra. Only nine were found, and all are fainter by at least 6.3 mag in the *G* band, so contamination from these objects is negligible.

### Light-curve analysis

Due to the number and variety of *TESS* data available for GK Dra, we investigated two choices with which to develop a model of the system. The first choice was to use only the 200-s-cadence data (sectors 56–60) as they have the highest available sampling rate; this was successful but led to a lower precision than desired in the final results. We therefore also modelled the 600-s-cadence data from sectors 47–55, augmented by the data from sectors 56–60 reduced to 600-s cadence for consistency.

In both cases we extracted the data within 0.6 d of an eclipse from the full datasets, in order to speed up the computation times in our analysis. The data around each eclipse were individually fitted with a straight line to normalize them to zero differential magnitude, and eclipses which were not fully covered by the data were rejected. This left us with 9730 data points (out of 53 296) for the 200-s light-curve and 10 497 data points (out of 47 378) for the 600-s light-curve. In both cases we ignored the error bars supplied with the *TESS* data as they do not account for the pulsations.

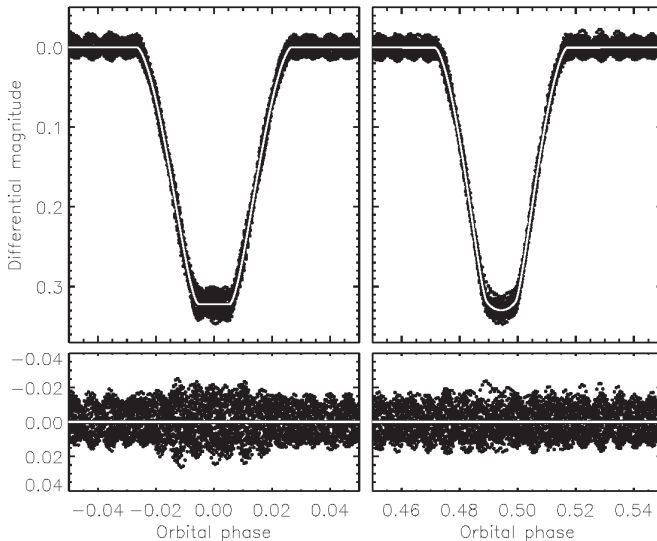


FIG. 2

The 600-s-cadence *TESS* light-curves of GK Dra (filled circles) and its best fit from JKTEBOP (white-on-black line) versus orbital phase. The primary eclipse is shown on the left and the secondary eclipse on the right. The residuals are shown on an enlarged scale in the lower panel.

\*<https://vizier.cds.unistra.fr/viz-bin/VizieR-3?-source=I/355/gaiadr3>

TABLE II

*Parameters of GK Dra measured from the TESS light-curves using the JKTEBOP code. The uncertainties are  $1\sigma$  and were determined using residual-permutation simulations. We give the results for both the 200-s- and 600-s-cadence data. We adopted the results for the 600-s-cadence data but with error bars double those reported in this table.*

Parameter	Value (200s)	Value (600s)
<i>Fitted parameters:</i>		
Primary eclipse time (BJD <sub>TDB</sub> )	2459905.05884 ± 0.00020	2459905.05884 ± 0.00024
Orbital period (d)	9.974128 ± 0.000053	9.974128 ± 0.000012
Orbital inclination (°)	88.27 ± 0.11	88.467 ± 0.062
Sum of the fractional radii	0.15687 ± 0.00065	0.15641 ± 0.00042
Ratio of the radii	1.791 ± 0.023	1.750 ± 0.010
Central-surface-brightness ratio	1.027 ± 0.048	0.938 ± 0.015
LD coefficient $c$	0.670 ± 0.086	0.584 ± 0.048
LD coefficient $\alpha$	0.448 (fixed)	0.448 (fixed)
$e \cos \omega$	-0.008985 ± 0.000041	-0.009000 ± 0.000036
$e \sin \omega$	-0.07811 ± 0.0021	-0.07998 ± 0.0017
<i>Derived parameters:</i>		
Fractional radius of star A	0.05620 ± 0.00028	0.05689 ± 0.00014
Fractional radius of star B	0.10067 ± 0.00087	0.09953 ± 0.00044
Light ratio $\ell_B/\ell_A$	3.30 ± 0.24	2.87 ± 0.073
Orbital eccentricity	0.0786 ± 0.0022	0.0805 ± 0.0017
Argument of periastron (°)	263.44 ± 0.18	263.58 ± 0.14

We modelled the light-curves using version 43 of the JKTEBOP\* code<sup>37,38</sup>. The fitted parameters included the sum ( $r_A + r_B$ ) and ratio ( $k = r_B/r_A$ ) of the fractional radii of the stars ( $r_A$  and  $r_B$ ), the central surface-brightness ratio ( $\mathcal{J}$ ), orbital inclination ( $i$ ), orbital period ( $P$ ), and a reference time of primary minimum ( $T_0$ ). The orbital eccentricity ( $e$ ) and argument of periastron ( $\omega$ ) were included as  $e \cos \omega$  and  $e \sin \omega$  to avoid their mutual correlation. Limb darkening was included in our model using the power-2 law<sup>39,40</sup>: we fitted for the  $c$  coefficients and fixed the  $\alpha$  coefficients to a theoretically-predicted value<sup>41,42</sup>. Third light was fixed at zero as attempts to fit it yielded a small negative value. The lower sampling rate of the 600-s-cadence data might bias the measurements of the fitted parameters<sup>43</sup>. We checked this by running fits where the model was numerically integrated to match the data<sup>43</sup>, finding a negligible change in the parameter values. We conclude that the sampling rate does not have a significant effect on the results given in Table II.

The depths of the primary and secondary eclipses are visually inseparable due to the similar  $T_{\text{eff}}$  values of the stars and the pulsational variability. However, our fits reliably converged to a situation in which the larger and more massive star is slightly cooler, in agreement with the results of ZW03. We therefore define star A to be the hotter but less massive star — it is the one eclipsed at the primary (deeper) eclipse. Star B is thus eclipsed at the secondary eclipse (which occurs at phase 0.4943) and is significantly larger and brighter than star A. The *TESS* data reveal that the eclipses are total<sup>†</sup>.

For the record, we were able to fit the light-curve quite well with the inverse of the ratio of the radii ( $k = 0.56$  in this case). This local-minimum solution could

\*<http://www.astro.keele.ac.uk/jkt/codes/jktebop.html>

†To be precise, the primary eclipse is total and the secondary eclipse is annular.

be rejected because the limb darkening caused curvature in the wrong eclipse (secondary *versus* primary) and thus did not match the data.

The uncertainties in the fitted parameters were determined using residual-permutation simulations<sup>44</sup>, treating the pulsational variation as red noise. Similar uncertainties were found by modelling the sectors of data individually<sup>45</sup>. See our recent paper on V1765 Cyg<sup>46</sup> for example plots from a similar residual-permutation analysis. The agreement between the results for the 200-s- and 600-s-cadence data is not as good as hoped, with differences between parameters of typically one to two times the size of the uncertainties. As we found above that the lower cadence of the 600-s data was not important, we adopted the results from these data but with the error bars doubled.

### Pulsation analysis

The *TESS* light-curve of GK Dra shows clear evidence for pulsations. The strongest frequency ( $f_8$ ) was detected in the RVs of star B by GBo3 so can be unambiguously attributed to that star. We fitted the 200-s-cadence data with JKTEBOP and subtracted the best-fitting model of the light-curve. The residuals of the fit were passed to version 1.2.0 of the PERIOD04 code<sup>47</sup> and a frequency spectrum was calculated from 0 to the Nyquist frequency of 216 d<sup>-1</sup>. No significant periodicity was found beyond 30 d<sup>-1</sup> (Fig. 3).

We measured a total of 15 significant frequencies in the frequency spectrum, adopting as our significance criterion a signal-to-noise ratio (S/N) greater than 4 (refs. 48, 49). We then fitted sinusoids simultaneously to all of them to obtain their amplitudes and phases. The uncertainties of the fitted parameters were calculated using both a standard least-square fit and Monte Carlo simulations, the latter being larger.

The results are given in Table III. We find three low frequencies ( $f_1$  to  $f_3$ ) near 0.46 d<sup>-1</sup> which are likely of the  $\gamma$  Doradus type. The strongest pulsation ( $f_8$ ) has a frequency of  $8.49070 \pm 0.00004$  d<sup>-1</sup> (period  $0.1177759 \pm 0.0000006$  d) and amplitude of 10.6 mmag; this is in wonderful agreement with the periodicity of  $0.1177753 \pm 0.0000005$  d found in the RVs of star B by GBo3. There are groups

TABLE III

*Significant pulsation frequencies found in the TESS 200-s-cadence light-curve of GK Dra after subtraction of the effects of binarity.*

Label	Frequency (d <sup>-1</sup> )	Amplitude (mmag)	Phase
$f_1$	$0.44029 \pm 0.00003$	$2.253 \pm 0.024$	$0.436 \pm 0.002$
$f_2$	$0.46049 \pm 0.00007$	$1.297 \pm 0.026$	$0.657 \pm 0.002$
$f_3$	$0.48624 \pm 0.00007$	$0.964 \pm 0.230$	$0.912 \pm 0.073$
$f_4$	$3.83445 \pm 0.00020$	$0.366 \pm 0.018$	$0.119 \pm 0.007$
$f_5$	$4.30136 \pm 0.00017$	$0.398 \pm 0.017$	$0.646 \pm 0.007$
$f_6$	$4.66593 \pm 0.00010$	$0.770 \pm 0.019$	$0.330 \pm 0.004$
$f_7$	$4.84289 \pm 0.00006$	$1.226 \pm 0.020$	$0.563 \pm 0.003$
$f_8$	$8.49070 \pm 0.00004$	$10.574 \pm 0.027$	$0.135 \pm 0.001$
$f_9$	$8.55349 \pm 0.00003$	$2.191 \pm 0.106$	$0.578 \pm 0.002$
$f_{10}$	$16.73503 \pm 0.00032$	$0.255 \pm 0.018$	$0.242 \pm 0.011$
$f_{11}$	$16.98151 \pm 0.00010$	$0.627 \pm 0.289$	$0.283 \pm 0.004$
$f_{12}$	$17.00896 \pm 0.00020$	$0.322 \pm 0.039$	$0.788 \pm 0.008$
$f_{13}$	$25.22548 \pm 0.00155$	$0.041 \pm 0.016$	$0.799 \pm 0.061$
$f_{14}$	$25.47241 \pm 0.00158$	$0.040 \pm 0.019$	$0.781 \pm 0.063$
$f_{15}$	$25.49961 \pm 0.00150$	$0.042 \pm 0.020$	$0.137 \pm 0.069$

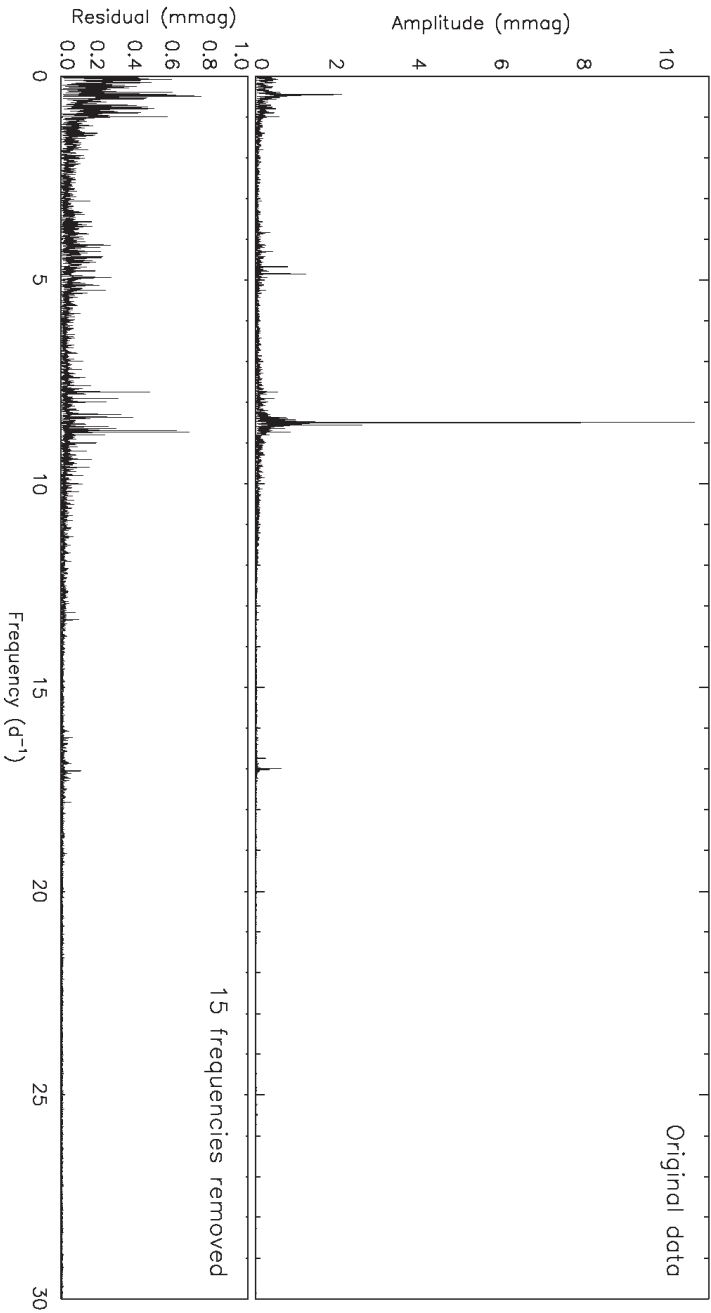


Fig. 3

Frequency spectrum of the *JESS* light-curve of GK Dra. Top: frequency spectrum of the data after subtraction of the binary model. Bottom: frequency spectrum after subtraction of the binary model and the 15 frequencies measured in this work.

of frequencies around  $3.8\text{--}4.8\text{ d}^{-1}$  ( $f_4$  to  $f_7$ ),  $8.5\text{ d}^{-1}$  ( $f_8$  and  $f_9$ ),  $16.7\text{--}17.0\text{ d}^{-1}$  ( $f_{10}$  to  $f_{12}$ ) and  $25.2\text{--}25.5\text{ d}^{-1}$  ( $f_{13}$  to  $f_{15}$ ), of the  $\delta$  Scuti type. The frequency spectrum of the residuals in Fig. 3 shows excess power in several frequency intervals, suggesting there are additional pulsations below our S/N criterion which might be measurable using additional data.

We conclude that the GK Dra system probably contains at least one hybrid  $\delta$  Sct /  $\gamma$  Dor star — the caveat here is that we know which is the pulsating star for only one of the frequencies so it is conceivable that one component produces the g-modes and the other the p-modes. Either way, this is an interesting system. None of the frequencies identified here correspond to multiples of the orbital frequency, so we find no evidence for tidally induced or perturbed pulsations. GK Dra has been observed for two sets of 13 consecutive sectors by *TESS*, with a third one scheduled, so is a good candidate for searching for amplitude modulation in a  $\delta$  Scuti star of known mass and radius<sup>50</sup>.

We also calculated frequency spectra of the 600-s-cadence data from sectors 47 to 60, expecting that the additional data would yield a cleaner spectrum with a lower noise floor. However, the resulting spectra all contained combs of aliases of the strongest frequencies separated by multiples of the orbital frequency; note that these were not seen in the 200-s data. This problem occurred using both the residuals of the JKTEBOP best fit, the original data, the original data with the eclipses removed, and the original data with the points during eclipse set to zero magnitude. GK Dra will benefit from a more detailed analysis in future, preferably including data from *TESS* sectors 73 to 83 that are scheduled for observation beginning in 2023 December.

#### Chromospheric emission

We obtained a spectrum of the Ca II *H* and *K* lines of GK Dra, alongside other objects in this series<sup>51,52</sup>, in order to probe for chromospheric emission lines indicative of magnetic activity. The current target was selected based on its Go spectral type listed in *Simbad*, which is much later than it should be (see above). GK Dra is thus not a promising target for chromospheric emission, but the spectrum only cost about 8 minutes of observing time.

The spectrum was obtained on the night of 2022/06/07 in excellent weather conditions, using the *Isaac Newton Telescope (INT)* and *Intermediate Dispersion Spectrograph (IDS)*, the 235-mm camera, the H2400B grating, the EEV10 CCD, a 1-arcsec slit, and an exposure time of 180 s. It covers 373–438 nm at a reciprocal dispersion of  $0.023\text{ nm px}^{-1}$  and a signal-to-noise ratio of approximately 150, and was taken at an orbital phase of 0.19. Data reduction was performed using a pipeline currently being written by the author<sup>53</sup>.

The spectrum is shown in Fig. 4, which also includes a synthetic spectrum for a  $T_{\text{eff}}$  of 7000 K and a  $\log g$  of 4.0 from the BT-Settl model atmospheres<sup>54,55</sup>. The Ca *H* and *K* line centres have a higher flux than those in the synthetic spectrum, but this can be attributed to the binarity (RV difference at the time of observation) and rotational velocities of the stars. Thus there is no clear evidence for chromospheric emission (as expected).

#### Physical properties of GK Dra

Based on the analysis presented above and published results for the system, we have determined the physical properties of GK Dra. We adopted the values of  $r_A$ ,  $r_B$ ,  $P$ , and  $i$  from the 600-s-cadence data in Table II, doubling the error bars as described above. For the velocity amplitudes of the system we used the

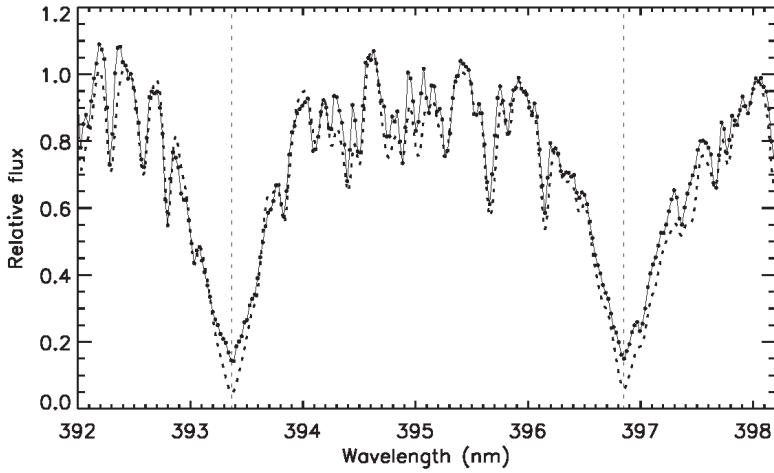


FIG. 4

Observed spectrum of GK Dra around the Ca II *H* and *K* lines (solid line with points) compared to a synthetic spectrum for a star with  $T_{\text{eff}} = 7000$  K,  $\log g = 4.0$ , and solar metallicity from the BT-Settl model atmospheres (dashed line) smoothed to the observed spectral resolution. The *H*- and *K*-line central wavelengths are shown with dotted lines. Both spectra have been normalized and shifted to zero velocity.

results from GB03 directly as these authors carefully accounted for the effects of pulsations in the RVs: we adopted  $K_A = 81.14 \pm 0.60$  km s<sup>-1</sup> and  $K_B = 64.97 \pm 0.13$  km s<sup>-1</sup> after interchanging the numbers to account for the differing definitions of which is the primary star. The  $T_{\text{eff}}$  values were taken directly from ZW03 — these correspond to spectral types of F1 and F2 on the calibration given by Pecaut & Mamajek<sup>57</sup> and are thus much earlier than the G0 given in the *Henry Draper Catalogue*<sup>21</sup>.

The physical properties were then calculated using the JKTDSDIM code<sup>58</sup> and entered into Table IV. The radii are measured to 0.7% (star A) and 1.0% (star B)

TABLE IV

*Physical properties of GK Dra defined using the nominal solar units given by IAU 2015 Resolution B3 (ref. 56). The  $T_{\text{eff}}$  values are from ZW03.*

Parameter	Star A	Star B
Mass ratio $M_B/M_A$		$1.249 \pm 0.010$
Semi-major axis of relative orbit ( $R_\odot^N$ )		$28.72 \pm 0.12$
Mass ( $M_\odot^N$ )	$1.421 \pm 0.012$	$1.775 \pm 0.028$
Radius ( $R_\odot^N$ )	$1.634 \pm 0.011$	$2.859 \pm 0.028$
Surface gravity ( $\log[\text{cgs}]$ )	$4.1642 \pm 0.0044$	$3.7749 \pm 0.0083$
Density ( $\rho_\odot$ )	$0.3257 \pm 0.0050$	$0.0760 \pm 0.0020$
Synchronous rotational velocity (km s <sup>-1</sup> )	$8.29 \pm 0.05$	$14.50 \pm 0.14$
Effective temperature (K)	$7100 \pm 70$	$6878 \pm 57$
Luminosity $\log(L/L_\odot^N)$	$0.786 \pm 0.018$	$1.217 \pm 0.017$
$M_{\text{bol}}$ (mag)	$2.774 \pm 0.045$	$1.698 \pm 0.042$
Distance (pc)		$306.9 \pm 4.8$

precision, limited by the results of the light-curve analysis, and the masses to 1.0% (star A) and 1.6% (star B) precision, limited by the effect of pulsations on the RVs of star B. The radius measurement of star A is very different from that of ZW03 ( $R_A = 2.431 \pm 0.042 R_\odot$ ) whereas for star B the values are consistent (ZW03 obtained  $R_B = 2.830 \pm 0.054 R_\odot$ ). This can be attributed to the extraordinary improvement in the quality of the *TESS* light-curve *versus* that previously available, and suggests the older error bars were significantly underestimated.

To test our results we determined the distance to GK Dra using the surface-brightness calibrations of Kervella *et al.*<sup>59</sup> for comparison with the *Gaia* parallax. We adopted the apparent magnitudes given in Table I, but with the 2MASS  $JHK_s$  values converted to the Johnson system<sup>60</sup>. Setting an interstellar reddening of zero gives consistent distances in the five passbands. The most precise is that in  $K_s$ ,  $306.9 \pm 4.8$  pc, which we adopt as our final value. This compares favourably with the *Gaia* DR3<sup>33,20</sup> parallax distance of  $303.5 \pm 1.2$  pc, suggesting that the radii and  $T_{\text{eff}}$  values in Table IV are reliable. As further evidence, the ratio of the  $T_{\text{eff}}$  values found by ZW03 is in perfect agreement with the surface-brightness ratio we found from the light-curve (Table II).

#### Comparison with theoretical models

GK Dra B shows significant evolution and is now cooler than GK Dra A despite its greater mass. We thus decided to compare the measured properties of GK Dra to the predictions of the PARSEC 1.2S theoretical stellar-evolutionary models<sup>61,62</sup>. The best fit was found in the mass–radius and mass– $T_{\text{eff}}$  diagrams<sup>63</sup> for an age of  $1400 \pm 50$  Myr and a fractional metal abundance of  $Z = 0.014$ . The age measurement is very sensitive to the properties of star B, and once the age is set the  $T_{\text{eff}}$  of star A is the primary determinant of the best  $Z$  value. The quoted age and  $Z$  provide an excellent match to the properties of star B, but star A is approximately  $2\sigma$  larger and hotter than predicted. A better agreement could be obtained by interpolation between the  $Z = 0.010$  and  $= 0.014$  models, but this is outside the scope of the current work.

We illustrate these results in a Hertzsprung–Russell diagram in Fig. 5. In this plot are a zero-age main sequence, evolutionary tracks for masses 1.2, 1.4, 1.6, 1.8, and  $2.0 M_\odot$ , and an isochrone for age 1400 Myr, all for a metal abundance of  $Z = 0.014$ . The isochrone provides a good but not perfect match to the properties of GK Dra.

#### Summary and conclusions

The eclipsing nature of GK Dra was discovered from *Hipparcos* photometry, and subsequent ground-based photometry and spectroscopy allowed the discovery of pulsations in the more massive star and approximate physical properties of this star and its companion. We have revisited GK Dra and used the extensive photometry available from the *TESS* mission to improve our understanding of the system. We find that the eclipses are total, and determine the masses and radii of the stars to high precision. These match the predictions of theoretical models for an age of 1.4 Gyr and a slightly subsolar metallicity.

The *TESS* data allow the detection and measurement of 15 significant pulsation frequencies, three of which are have low frequencies in the region of  $0.5 \text{ d}^{-1}$  so arise from the  $\gamma$  Dor phenomenon, and the remaining 12 of which form four groups of higher frequencies consistent with  $\delta$  Scuti pulsations. By far the strongest frequency is at  $f_8 = 8.49 \text{ d}^{-1}$ , and this one has been detected

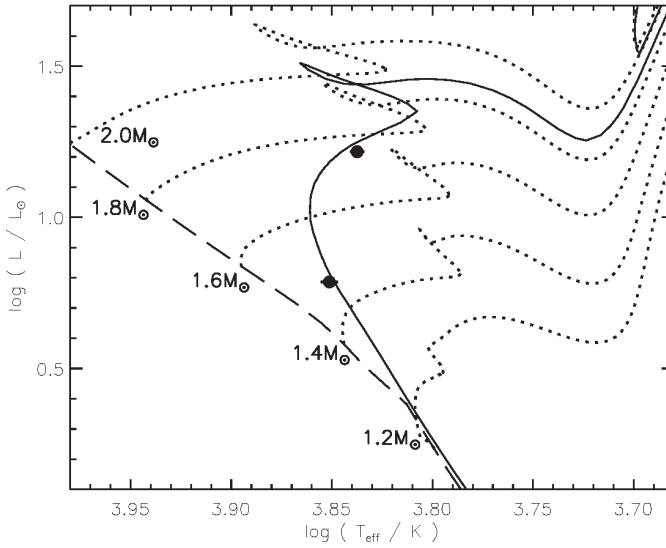


FIG. 5

Hertzsprung–Russell diagram for the components of GK Dra (filled circles with error bars) and the predictions of the PARSEC 1:2S models for selected masses (dotted lines with masses labelled) and the zero-age main sequence (dashed line), for a metal abundance of  $Z = 0.014$ . The 1.4-Gyr isochrone is shown with a solid line.

spectroscopically in the more evolved star B. GK Dra almost certainly contains one or two hybrid  $\gamma$  Dor/ $\delta$  Sct stars, and more extensive data are expected to reveal further pulsation frequencies.

The measured properties of GK Dra are now sufficiently precise and accurate to be included in the *Detached Eclipsing Binary Catalogue (DEBCat\**, ref. 64). *TESS* is scheduled to observe GK Dra between 2023 December and 2024 September. A detailed asteroseismic analysis of these data, once available, is recommended.

#### Acknowledgements

We thank the anonymous referee for a positive report. This paper includes data collected by the *TESS* mission and obtained from the MAST data archive at the Space Telescope Science Institute (STScI). Funding for the *TESS* mission is provided by the NASA’s Science Mission Directorate. STScI is operated by the Association of Universities for Research in Astronomy, Inc., under NASA contract NAS 5–26555. This work has made use of data from the European Space Agency (ESA) mission *Gaia*<sup>†</sup>, processed by the *Gaia* Data Processing and Analysis Consortium (DPAC<sup>‡</sup>). Funding for the DPAC has been provided by national institutions, in particular the institutions participating in the *Gaia* Multilateral Agreement. The following resources were used in the course of this work: the NASA Astrophysics Data System; the *Simbad* database operated at CDS, Strasbourg, France; and the arXiv scientific paper preprint service operated by Cornell University.

\*<https://www.astro.keele.ac.uk/jkt/debcats/>

†<https://www.cosmos.esa.int/gaia>

‡<https://www.cosmos.esa.int/web/gaia/dpac/consortium>

## References

- (1) J. Higl & A. Weiss, *A&A*, **608**, A62, 2017.
- (2) A. Claret & G. Torres, *ApJ*, **859**, 100, 2018.
- (3) A. Tkachenko *et al.*, *A&A*, **637**, A60, 2020.
- (4) C. Aerts, J. Christensen-Dalsgaard & D. W. Kurtz, *Asteroseismology* (Springer), 2010.
- (5) C. Aerts *et al.*, *Science*, **300**, 1926, 2003.
- (6) M. Briquet *et al.*, *MNRAS*, **381**, 1482, 2007.
- (7) A. García Hernández *et al.*, *A&A*, **559**, A63, 2013.
- (8) T. R. Bedding *et al.*, *Nature*, **581**, 147, 2020.
- (9) J. Southworth, *Universe*, **7**, 369, 2021.
- (10) P. Gaulme & J. A. Guzik, *A&A*, **630**, A106, 2019.
- (11) X. Chen *et al.*, *ApJS*, **263**, 34, 2022.
- (12) F. Kahraman Aliçavuş *et al.*, *MNRAS*, **524**, 619, 2023.
- (13) M. Breger, in *Delta Scuti and Related Stars* (M. Breger & M. Montgomery, ed.), 2000, *Astronomical Society of the Pacific Conference Series*, vol. 210, pp. 3–42.
- (14) A. Grigahcène *et al.*, *ApJ*, **713**, L192, 2010.
- (15) J. Debosscher *et al.*, *A&A*, **556**, A56, 2013.
- (16) J. Southworth & T. Van Reeth, *MNRAS*, **515**, 2755, 2022.
- (17) G. W. Henry, F. C. Fekel & S. M. Henry, *AJ*, **133**, 1421, 2007.
- (18) L. A. Balona, J. Daszyńska-Daszkiewicz & A. A. Pamyatnykh, *MNRAS*, **452**, 3073, 2015.
- (19) J. Southworth, *The Observatory*, **140**, 247, 2020.
- (20) Gaia Collaboration, *A&A*, **649**, A1, 2021.
- (21) A. J. Cannon & E. C. Pickering, *Annals of Harvard College Observatory*, **96**, 1, 1921.
- (22) K. G. Stassun *et al.*, *AJ*, **158**, 138, 2019.
- (23) E. Høg *et al.*, *A&A*, **355**, L27, 2000.
- (24) R. M. Cutri *et al.*, *2MASS All Sky Catalogue of Point Sources* (The IRSA 2MASS All-Sky Point Source Catalogue, NASA/IPAC Infrared Science Archive, Caltech, US), 2003.
- (25) ESA (ed.), *The Hipparcos and Tycho catalogues. Astrometric and photometric star catalogues derived from the ESA Hipparcos space astrometry mission*, *ESA Special Publication*, vol. 1200, 1997.
- (26) E. V. Kazarovets *et al.*, *IBVS*, **4659**, 1, 1999.
- (27) S. Dallaporta *et al.*, *IBVS*, **5312**, 1, 2002.
- (28) A. Liakos & P. Niarchos, *MNRAS*, **465**, 1181, 2017.
- (29) F. Kahraman Aliçavuş *et al.*, *MNRAS*, **470**, 915, 2017.
- (30) R. F. Griffin & H. M. J. Boffin, *The Observatory*, **123**, 203, 2003.
- (31) P. F. L. Maxted *et al.*, *A&A*, **578**, A25, 2015.
- (32) T. Zwitter *et al.*, *A&A*, **404**, 333, 2003.
- (33) Gaia Collaboration, *A&A*, **595**, A1, 2016.
- (34) G. R. Ricker *et al.*, *Journal of Astronomical Telescopes, Instruments, and Systems*, **1**, 014003, 2015.
- (35) Lightkurve Collaboration, ‘(Lightkurve: Kepler and TESS time series analysis in Python)’, Astrophysics Source Code Library, 2018.
- (36) J. M. Jenkins *et al.*, in *Proc. SPIE*, 2016, *Society of Photo-Optical Instrumentation Engineers (SPIE) Conference Series*, vol. 9913, p. 99133E.
- (37) J. Southworth, P. F. L. Maxted & B. Smalley, *MNRAS*, **351**, 1277, 2004.
- (38) J. Southworth, *A&A*, **557**, A119, 2013.
- (39) D. Hestroffer, *A&A*, **327**, 199, 1997.
- (40) J. Southworth, *The Observatory*, **143**, 71, 2023.
- (41) A. Claret & J. Southworth, *A&A*, **664**, A128, 2022.
- (42) A. Claret & J. Southworth, *A&A*, **674**, A63, 2023.
- (43) J. Southworth, *MNRAS*, **417**, 2166, 2011.
- (44) J. Southworth, *MNRAS*, **386**, 1644, 2008.
- (45) J. Southworth, *The Observatory*, **141**, 234, 2021.
- (46) J. Southworth, *The Observatory*, **143**, 254, 2023.
- (47) P. Lenz & M. Breger, *Communications in Asteroseismology*, **146**, 53, 2005.
- (48) M. Breger *et al.*, *A&A*, **271**, 482, 1993.
- (49) R. Kuschnig *et al.*, *A&A*, **328**, 544, 1997.
- (50) D. M. Bowman *et al.*, *MNRAS*, **460**, 1970, 2016.
- (51) J. Southworth, *The Observatory*, **142**, 267, 2022.
- (52) J. Southworth, *The Observatory*, **143**, 19, 2023.
- (53) J. Southworth *et al.*, *MNRAS*, **497**, 4416, 2020.
- (54) F. Allard *et al.*, *ApJ*, **556**, 357, 2001.
- (55) F. Allard, D. Homeier & B. Freytag, *Phil. Trans. Series A*, **370**, 2765, 2012.
- (56) A. Prša *et al.*, *AJ*, **152**, 41, 2016.
- (57) M. J. Pecaut & E. E. Mamajek, *ApJS*, **208**, 9, 2013.
- (58) J. Southworth, P. F. L. Maxted & B. Smalley, *A&A*, **429**, 645, 2005.
- (59) P. Kervella *et al.*, *A&A*, **426**, 297, 2004.

- (60) J. M. Carpenter, *AJ*, **121**, 2851, 2001.  
 (61) A. Bressan *et al.*, *MNRAS*, **427**, 127, 2012.  
 (62) Y. Chen *et al.*, *MNRAS*, **444**, 2525, 2014.  
 (63) J. Southworth & J. V. Clausen, *A&A*, **461**, 1077, 2007.  
 (64) J. Southworth, in *Living Together: Planets, Host Stars and Binaries* (S. M. Rucinski, G. Torres & M. Zejda, eds.), 2015, *Astronomical Society of the Pacific Conference Series*, vol. 496, p. 321.

---

## REVIEWS

**Supermassive Black Holes**, by Andrew King (Cambridge University Press), 2023. Pp. 308, 25 × 17.5 cm. Price £54.99/\$69.99 (hardbound; ISBN 978 1 108 48805 1).

Recently, supermassive black holes have garnered significant attention, captivating both the public and scientists alike. The no-hair theorem states that any black hole can be completely described by its mass, angular momentum, and charge; nevertheless, a multitude of intricate phenomena emerge from these systems. The past decade has seen ground-breaking advances, such as the direct detection of gravitational waves from merging stellar-mass and intermediate-mass black holes as well as the imaging of black-hole shadows by the *Event Horizon Telescope*.

Looking towards the future, black-hole science holds immense promise, especially with electromagnetic facilities such as *JWST* pushing detections of supermassive black holes to higher redshifts, and next-generation gravitational-wave detectors, such as *LISA* and *IPTA*, targeting the supermassive black-hole regime. Notably, strong observational hints at a gravitational-wave background formed from the cosmic population of supermassive binary black holes detected by *IPTA* have further intensified the excitement.

Amidst this backdrop, Andrew King's book, *Supermassive Black Holes*, proves to be a timely and relevant textbook in the current research landscape. It masterfully weaves together the theories of General Relativity and fluid dynamics with the rich phenomenology of active galactic nuclei (AGN) and the co-evolution of supermassive black holes and their host galaxies. The book comprises eight chapters, where the initial four lay the essential groundwork for the cutting-edge research topics explored in the latter four.

In the first chapter, the author outlines crucial theoretical concepts and observational characteristics of supermassive black holes. Moving on, the second chapter serves as a summary of the salient features of General Relativity concerning black holes, catering to both those familiar with GR and newcomers. The third chapter focusses on astrophysical gasses, encompassing fluid dynamics in various relevant regimes, including incompressible flows, shocks, plasma theory, and magnetohydrodynamics. The author establishes connections to different astrophysical scenarios, discussing the applicability of standard approximations while cautioning against quasi-Newtonian treatments. Chapter 4 delves into accretion-disc theory, starting with Newtonian orbits

and subsequently connecting them to previously discussed GR solutions. A detailed examination of the thin-disc model follows, with attention to other disc types, particularly in the super-Eddington regime (slim discs and advection-dominated accretion flows). The chapter concludes by addressing accretion-flow simulations and associated numerical pitfalls.

The second half of the book delves into frontier research topics. Chapter 5 covers various theoretical aspects of black-hole growth, including gas-transport mechanisms and chaotic accretion. It extensively discusses misaligned accretion discs, applying the same theory to circumbinary discs and their significant role in orbital shrinking and the final-parsec problem. Tidal-eruption events and the novel field of quasi-periodic eruptions are also explored, with the latter potentially providing crucial insights into low-mass black holes. Chapter 6 is a deep dive into the black-hole–galaxy scaling relations, with a focus on the AGN wind-driven scenario, supplemented by alternative explanations like deriving scaling relations from the assembly history. Observational constraints, especially from AGN in dwarf galaxies, are also analyzed. Chapter 7 reviews other forms of AGN feedback, in particular radiatively-driven winds and jets. Different jet-production mechanisms and jet precession are discussed from both observational and theoretical perspectives. The book concludes with Chapter 8, which broadly addresses ‘black-hole growth’ and the process of constraining different theoretical models through observations, including the AGN luminosity function, supermassive-black-hole-mass limits, and deviations from the scaling relations. Each chapter includes problem sets for further engagement.

Personally, I found the book to be a highly enjoyable read, offering a comprehensive overview of crucial theoretical concepts related to supermassive black holes. Andrew King presents the material in an accessible manner, making it particularly well-suited for graduate students embarking on their journey in this field. Additionally, advanced undergraduates seeking background reading for research projects could find this book valuable. It is also an excellent resource for individuals transitioning from a general physics background to astrophysics, as it illuminates the connections between General Relativity, fluid dynamics, and the intricate world of AGN physics. As I pass the book on to my summer student, I wholeheartedly recommend it to anyone interested in exploring the fascinating world of supermassive black holes. — SOPHIE KOUDMANI.

**Simulating the Cosmos. Why the Universe Looks the Way it Does,**

by Romeel Davé (Reaktion), 2023. Pp. 199, 22.5 × 14.5 cm. Price £15.95 (hardbound; ISBN 978 1 78914 714 8).

Who would have thought that a book on numerical modelling could be such fun! A leading practitioner of the art, Davé demystifies the black boxes of N-body simulations, hydrodynamical modelling, and the rest in irreverent style, exemplified, perhaps, by the final sentence of Chapter 1, prior to embarking on modelling the Universe: “To do this, we’re going to need computers. Big ones.” The first chapter itself sprints through the development of cosmology, both observational and theoretical, from Hubble and Lemaître through the CMB and inflation to the concordance model of  $\Lambda$ CDM in 40 pages. While unsurprisingly light on the nuances of the history, this provides an excellent background for the later chapters on ‘Putting the Universe on a Computer’ and on the ever-improving simulations of large-scale structure and the formation and evolution of galaxies (including a section ‘Are We There Yet?’). The easy-

going style means that you are soon reading about time steps and particle-mesh codes without realizing that it's become more technical. At the end, there is even room for a discussion of whether we live in a simulation. References to academic papers are provided for those wishing to dive in deeper, but this is essentially the nearest you can get to light reading on numerical cosmology. Highly recommended — especially given the remarkable price for a hardback these days. — STEVE PHILLIPPS.

**The End of Everything (Astrophysically Speaking)**, by Katie Mack (Penguin), 2021. Pp. 238, 19.5 × 13 cm. Price £9.99 (paperback; ISBN 978 0 141 98958 7).

Katie Mack has “[bounced] back and forth between physics and astronomy departments, studying black holes, galaxies, intergalactic gas, intricacies of the Big Bang, dark matter, and the possibility that the universe might suddenly blink out of existence” and “even dabbled in experimental particle physics for a while”; she now holds the Hawking Chair in Cosmology and Science Communication at the Perimeter Institute for Theoretical Physics in Canada and has written many popular-science pieces in various media, though this is her first book. There are many books, from popular-science books to technical monographs, about the origin of the Universe, but comparatively few about the possible ways it might end. After an introduction and summary of the history of the Universe from the Big Bang until now, she looks at five ways the Universe could end: Big Crunch, Heat Death, Big Rip, vacuum decay, and bounce.\* The final chapter before the Epilogue starts with a discussion of a paper<sup>7</sup> in this *Magazine* by the later Astronomer Royal Martin Rees, ‘The collapse of the Universe: an eschatological study’. (At that time, a Big Crunch seemed most likely — though Rees also touched on a ‘conventional’ Big Bounce — but today that seems to be the least likely possibility.) That is followed by a look at Dyson’s view<sup>8</sup> assuming that the Universe will expand forever before current (and future) experiments and various ideas about where theory might be heading are discussed. The Epilogue features Rees again and other scientists talking about their personal feelings regarding the end of the Universe.

On the whole, the book does its job well, giving a popular-science-level introduction to some ways in which the Universe could end (as well as a summary of its history). Many readers might not have heard of the Big Rip or vacuum decay, and those are explained clearly and well. My main gripe is that it gets some things wrong regarding traditional observational cosmology. While it is not uncommon for confusion to arise from over-simplification, that shouldn’t be a problem for a professional science communicator. The problem is not a new one: confusion related to ‘the redshift–distance and velocity–distance laws’.<sup>†</sup> At the latest after the publications of Harrison’s paper<sup>9</sup> with that title, no-one should still be confused, but many, even some professionals, are.<sup>10</sup> The Hubble–Lemaître law, that recession velocity is proportional to

\*Tegmark<sup>1,2</sup> (the latter reviewed in these pages<sup>3</sup>) also discusses five ways in which the Universe might end: Big Chill (Heat Death), Big Crunch, Big Rip, Big Snap (can occur if the fabric of space is not infinitely stretchable), and Death Bubbles (vacuum decay; also known as the Big Slurp), but not a bouncing Universe. Of course, in some sense a bouncing Universe doesn’t end, but the main reason for the difference is probably that the Big Snap has not been discussed as much as the other four, while the old idea of a bouncing or, in general, cyclic Universe (*e.g.*, ref. 4) has become more popular recently in the context of the ekpyrotic model<sup>5</sup> and Conformal Cyclic Cosmology<sup>6</sup>.

<sup>†</sup>The second footnote on p. 58 provides almost a textbook example of the confusion Harrison<sup>9</sup> addresses.

proper distance\*, is extremely simple: it is the only velocity–distance law for which a homogeneous and isotropic universe remains so. (Note that that is pure kinematics; no dynamics, much less physics, let alone General Relativity, is needed.) The dependence of (various sorts of) distance on redshift is in general complicated, and observational cosmology works by comparing an observed distance–redshift relation (the distance is hard to measure accurately; the redshift is easy) to those calculated for various combinations of the cosmological parameters. Velocities play no role. While it is true that knowing the expansion history of the Universe ( $H(z)$ , where  $H$  is the Hubble constant and  $z$  the redshift) allows one to determine the cosmological parameters  $\Omega$  and  $\lambda$  (the density parameter and normalized cosmological constant, respectively) and *vice versa*, one cannot actually measure the expansion velocity at high redshift. Thus, Mack’s scheme (p. 59) of determining the expansion history by measuring  $z$  and using the Hubble–Lemaître law to get the distance and then using that distance to determine the light-travel time and hence the time the light was emitted won’t work: Measuring  $z$  gives us the velocity only if we already know the cosmological parameters (by using them to calculate the distance and then, *via* the Hubble–Lemaître law, to *calculate* the velocity), and similarly the light-travel time can be calculated only if the cosmological parameters are known. (Of course, in general the light-travel-time distance is not the same as the luminosity distance or angular-size distance which are the distances most commonly used in observational cosmology, though knowing the cosmological parameters allows one to calculate them all.) On p. 62, she claims that if the Universe collapses, then the Hubble–Lemaître law is valid “right up until the expansion stops completely”. No. The Hubble–Lemaître law is *always* valid (at least in a Friedmann model, which is the context here). “Right now, the more distant an object, the faster it recedes [true] and therefore, the higher the redshift [not in general] (the Hubble–Lemaître law.)” She claims that we would “*perceive* distant objects as still receding long after they start turning around” [her italics]. We cannot ‘perceive’ velocity. We can measure redshift, but cannot (except in the limit of small redshift) convert that to a velocity without additional knowledge or assumptions. The Hubble–Lemaître law still applies, but it connects velocity with distance, not with redshift. On p. 69, she notes, correctly, that to know whether the Universe will collapse (by knowing the cosmological parameters), we must know the expansion history. True. That involves measuring distance, which is difficult. True. But the claim that galaxy velocities “can be determined with redshift measurements” at large redshift is just plain wrong. As described above, we can calculate them if we know the distance as a function of redshift, but if we know that, we don’t actually need the velocities. On pp. 72–73 she again implies that not only distance measurements but also velocity measurements are part of observational cosmology. The

\*Hubble himself used low-redshift data (many from Slipher and uncredited). At low redshift, one can use apparent magnitude as a proxy for distance (luminosity distance, but in the limit of low redshift all distance measures are equivalent) and redshift as a proxy for velocity, thus Hubble<sup>11</sup> could correctly speak of the observations supporting ‘A Relation between Distance and Radial Velocity among Extra-Galactic Nebulae’, since he was working only at low redshift. What he actually observed is a correlation between apparent magnitude (for sources of presumably similar absolute magnitude) and redshift. Although there is some variation in how the terminology is (ab)used, the consensus is that the Hubble–Lemaître law refers to the correlation between distance and radial velocity, as in the title of Hubble’s article (the velocity–distance law), although that is not what he observed. (The redshift–distance law — in general, a different law for different distances which also depends on the cosmological parameters — is neither a simple law nor named after anyone.)

latter are neither possible nor needed. Again on p. 74 (discussing supernova cosmology), she claims that one needs distance and velocity as a function of redshift; the former is sufficient. On p. 185 it is again repeated that *measurement* of the velocities of high-redshift supernovae are needed to derive the expansion history of the Universe; the reverse is true, and velocities are not needed as input into any other calculations. In any case, the redshift cannot indicate “how quickly cosmic expansion is happening at that point” without already knowing the cosmological parameters. Velocities, measured or calculated, are not used in observational cosmology at all. On p. 191, redshift drift (*e.g.*, ref. 12 and references therein) is mentioned, but confusingly cast in terms of “apparent velocity”.

I have dwelt on that confusion because it demonstrates, yet again, that some who really should know better still get it wrong. Also, such popular-science books are read by many more people than those who read technical textbooks, the former sometimes providing an introduction to the latter. The reader then must understand the confusion, and the impression left is that of sloppiness. It’s worth it to get it right, whatever the context. Other errors are minor: I don’t think that Einstein “reluctantly” gave up the cosmological constant when he learned that the Universe is expanding; by all accounts he was more than happy to do so, whether or not he actually described it as his ‘biggest blunder’<sup>13</sup>. The Hubble radius is sometimes confused with the event horizon (ref. 14 sets the record straight, although that should have been clear since Rindler’s classic paper<sup>15</sup>). Entropy is not the only part of physics which cares about the arrow of time<sup>16,17</sup>. A universe with a (positive) cosmological constant can (but doesn’t have to; it depends on the value) accelerate not only if its spatial geometry is flat, but also in the positively and negatively curved cases. A couple of things (the relationship between geometry and destiny and Hawking radiation) are presented more or less correctly, but only after repeating the common special-case version (for the former) or a completely wrong explanation (for the latter, though here the wrong version is presented explicitly to contrast it with the proper explanation).

The production is fine except for the black-and-white figures in which too-light shades of grey are very difficult to make out (perhaps black-and-white versions of colour figures?). Typos are few and annoying matters of style too many but nevertheless about average for most books I read. There are fortunately footnotes rather than end notes. There is no bibliography as such, though a few papers are mentioned by author and title in the main text. The book ends with three pages of acknowledgements and a ten-page small-print index.

Despite the goofs mentioned above (which some readers might recognize and forgive), I can nevertheless recommend the book, since otherwise it is well written and provides a popular-level introduction to a topic which is usually reserved for more technical literature (*e.g.*, refs. 1, 7, 18–20). — PHILLIP HELBIG.

### References

- (1) M. Tegmark, *Phys. Rev. D.*, **85**, 123517, 2012.
- (2) M. Tegmark, *Our Mathematical Universe* (Allen Lane), 2014.
- (3) P. Helbig, *The Observatory*, **134**, 150, 2014.
- (4) S. J. Gould, *Time’s Arrow, Time’s Cycle: Myth and Metaphor in the Discovery of Geological Time* (Harvard University Press), 1987.

- (5) J. Khoury *et al.*, *Phys. Rev. D.*, **64**, 123522, 2001.
- (6) R. Penrose, *Cycles of Time: An Extraordinary New View of the Universe* (Bodley Head), 2010.
- (7) M. Rees, *The Observatory*, **89**, 972, 1969.
- (8) F. J. Dyson, *Rev. Mod. Phys.*, **51**, 447, 1979.
- (9) E. R. Harrison, *ApJ*, **403**, 28, 1993.
- (10) P. Helbig, *The Observatory*, **138**, 22, 2018.
- (11) E. Hubble, *Proc. Nat. Acad. Sci. USA*, **15**, 168, 1929.
- (12) P. Helbig, *MNRAS*, **519**, 2769, 2023.
- (13) C. O’Raifeartaigh & S. Mitton, *Physics in Perspective*, **20**, 318, 2018.
- (14) P. van Orschot, J. Kwan & G. F. Lewis, *MNRAS*, **404**, 1633, 2010.
- (15) W. Rindler, *MNRAS*, **116**, 6, 1956.
- (16) B. W. Roberts, *Reversing the Arrow of Time* (Cambridge University Press), 2022.
- (17) P. Helbig, *The Observatory*, **143**, 238, 2023.
- (18) A. S. Eddington, *Nature*, **127**, 447, 1931.
- (19) J. Barrow & F. Tipler, *The Anthropic Cosmological Principle* (Oxford University Press), 1988.
- (20) F. C. Adams & G. Laughlin, *Rev. Mod. Phys.*, **69**, 337, 1997.

**Solar Surveyors: Observing the Sun from Space**, by Peter Bond (Springer), 2022. Pp. 535, 24 × 16.5 cm. Price £29.99 (paperback; ISBN 978 3 030 98787 9).

*Solar Surveyors* is a very comprehensive overview of mostly space-based solar and interplanetary missions dating from the earliest rocket launches to study solar X-ray and ultraviolet emission in the years following World War II to the latest probes still operating. There is a long introductory passage giving the reader the fundamentals of solar physics, including solar radiation and the nuclear source of solar energy, as well as the history of the subject dating back to the time of Newton and Herschel. There is a well-illustrated section on ground-based observatories including the latest telescope in Hawaii with an outline of the helioseismology *GONG* network, followed by how the early rocket-borne instruments enabled solar astronomers to investigate the nature of the high-temperature solar corona and solar flares.

A discussion of interplanetary probes takes the reader on to the meat of the book, the space observatories looking at the Sun from low-Earth orbit to those viewing the Sun from interplanetary probes. Examples include the high-energy X-ray mission *RHESSI*, the two *STEREO* spacecraft and Japanese *Hinode* spacecraft, and *Solar Orbiter*, which is still about to obtain images of the polar regions of the solar corona as well as hard-X-ray images of flares.

Nearly all the references are to web sites rather than journal articles, which could be a little dangerous as web sites are liable to change with time. I did some spot checks and they seemed to be still valid. I am familiar with many of the missions listed and found at least one (to the *Coronas F* mission) where the wavelength ranges are wrong, apparently by a factor ten because of an erroneous Ångström-to-nanometre conversion.

Although the book is very well illustrated, some of the figures seem to have come from an imperfect reproduction of those in web sites.

The book would be very useful to those who are writing introductions to their PhD theses and perhaps the general reader who wishes to be familiar with the history of space solar physics, although the level of detail may be a little off-putting. — KEN PHILLIPS.

## THESIS ABSTRACT

SPECTRAL ENERGY DISTRIBUTION MODELLING OF X-RAY-SELECTED AGNS  
AND THEIR HOST GALAXIES

*By Adam Marshall*

The nature of the relation between active galactic nuclei (AGN), and their host galaxies has been observed in detail throughout the Universe. Such work has found an intrinsic link between central supermassive-black-hole (SMBH) masses, and host-galaxy properties such as the velocity dispersion of stars, and bulge mass. However, the difference in scale between SMBH and their host galaxies has led to debate on how this relation might form and develop over time. In order to aid in understanding the relation between AGN and their host galaxies, the work throughout this thesis has therefore focussed on the development and implementation of a new spectral-energy-distribution (SED) fitting code, using an up-to-date AGN SED to infer accurately both AGN and host-galaxy properties. To this end, we explore the intricacies involved in producing useful property inferences using a Bayesian MCMC fitting method, whilst working to avoid common issues such as bimodality and lack of convergence. We then perform SED fitting using our methods to 711 luminous X-ray AGN at  $0.7 < z < 4.5$  using 10 bands of optical and infrared photometric data for objects within *XMM-SERVS*. Using these fits, we study the relation between AGN X-ray luminosity and host-galaxy stellar mass, along with our ability to predict emission-line strength and morphology from photometry alone. In order to understand further the intricacies of SED fitting, we also provide a case study into the effect of AGN-SED choice on host-galaxy and AGN-property inferences by comparing our AGN SED to another commonly used template. In this work, we show that it is important to consider host-galaxy contamination when trying to produce a pure AGN template, and the effect that this contamination can have on AGN and host-galaxy-property inferences. We also find that the use of lower-resolution SEDs can lead to repercussions on property inferences such as host-galaxy stellar mass, which may provide incorrect assumptions on the relation between AGN and their host galaxies. — *University of Cambridge; accepted 2023 February.*

---

## OBITUARY

*Phillip John David Gething (1929–2023)*

Phillip was born on 1929 August 22 and brought up in Luton, where he attended Luton Grammar School from 1939 to 1946. He won a Royal Scholarship to Imperial College and in 1946 October, at the age of 17, began a compressed two-year course for a maths degree in the company of many ex-servicemen and a few school leavers. A third year was compulsory for school leavers so, having become increasingly interested in astronomy, he chose the MSc course in optics and then returned to the maths department as a PhD student under Dr. Whitrow from 1949–51.

For his PhD research, Phillip looked at various problems concerning the origin of cosmic rays and comets, and the applications of kinematic relativity to cosmology, and had three papers published, the most substantial in the *Proceedings of the Royal Society*.

By good fortune, scientific posts at the Royal Observatory were being advertised as he completed his thesis. Phillip started work in the Meridian Department at Greenwich in August, as the first-ever Scientific Officer employed there under a new grading system for the whole of the scientific civil service. His duties involved a mixture of observing, arithmetic, and research investigations. In 1952 he joined the Royal Astronomical Society, and remained a Fellow for the rest of his life — over 71 years of membership! From 1954 to 1956 Phillip was on the editorial board of *The Observatory*. He also became a member of a commission of the International Astronomical Union concerned with comets.

Phillip married Helen Slater in 1953, and they started their married life in Highmore Road, Blackheath. Their elder son, David, was born in Greenwich.

Then the transfer to Herstmonceux Castle in 1954, living first in a rented bungalow in Pevensey Bay and then in a council house in Herstmonceux village, where younger son Martin was born. Phillip supervised the installation of a new instrument, the *Photographic Zenith Tube*, then organized the observing routines and methods of calculation to derive accurate time and latitude: he found this a most interesting project. He played bridge with the new Astronomer Royal, Dr. Woolley, attended lectures in Oxford with him and Tommy Gold, and found time to play chess in a tournament in Hastings.

After a time Phillip began to find the routine calculations and irregular observing duties were losing their appeal. He came under pressure from Woolley to spend a few years in South Africa, at the Royal Observatory at the Cape, but was not willing to do so. Eventually he asked for a change, and accepted a transfer to Government Communications HQ in Cheltenham in 1957. There Phillip and Helen were able to buy their first house and for the next 18 years he enjoyed his work in the Science and Engineering Division. In 1970 he received an 'Individual Merit' promotion that freed him from routine administrative duties in order to give more time for research.

Throughout his time in GCHQ Phillip worked on radio propagation, radio direction finding, and the design of improved antenna arrays. He also ran a number of contracts with industry and universities, sometimes acted as external examiner for candidates seeking higher degrees, and was able to publish several scientific papers in the open literature. He made many visits to the USA and organized a comparison trial of rival direction finders used by the US Air Force and the US Navy, and wrote the report on the results.

By 1975, when both sons had departed to university, Phillip felt that he had done all he could in his chosen fields and that he ought to get back into the main management stream. He transferred to the Admiralty Compass Observatory, Slough, where he looked at problems of integrated navigation for the Royal Navy: his background in astronomy and in radio position-fixing techniques proved useful.

Soon after, Phillip was appointed as head of the computer-techniques division at the parent Admiralty Research Establishment near Portsmouth, and the family moved to Waterlooville in 1977. His team was mainly concerned with the use of computers at sea for Command and Control systems, and they worked very closely with the Royal Navy — the Falklands Campaign in 1982 showing the importance of their work.

In 1983 Phillip transferred to the Ministry of Defence (MoD) headquarters in London as Assistant Director of Defence Procurement for cryptographic devices and strategic communications systems. He and Helen moved to Fleet, from where he could commute to London by train each day. He became project manager for a number of major contracts to develop and install new systems for the RAF, including the command centre at High Wycombe.

At the end of 1987 Phillip took early retirement from the Civil Service and joined Admiral Management Services in Camberley as a management consultant. He put together a successful bid for a multi-million-pound contract with GCHQ and was then appointed as the facility manager for a software evaluation facility, looking particularly at security issues on behalf of the MOD.

Phillip retired in 1989 but continued giving occasional lectures at the Royal Military College of Science, and was external supervisor for an Australian officer working on a Direction Finding project as part of his MSc course. He kept busy throughout his retirement: serving on the management committee of Fleet Citizens Advice Bureau for 13 years, and as lay member of the medical ethics committee for North and Mid Hampshire, with monthly meetings at the Royal Hampshire Hospital in Winchester.

Chess had been one of his main hobbies from school days onwards, and in various periods Phillip had represented Bedfordshire, Gloucestershire, and Hampshire in county matches. He also enjoyed creative writing, and belonged to writing circles in Slough, Waterlooville, and Fleet. He had a number of short stories and articles published, and one-act plays performed.

Phillip and Helen celebrated their golden wedding anniversary in 2003. However, Helen's health began to fail and she passed away the following year. Phillip died peacefully on 2023 July 12 and is survived by two sons, four grandchildren, and three great-grandchildren. — MARTIN GETHING.

---

*Here and There*

JUST MISSING A MILLION?

R136a is, of all the stars known to astronomy, the brightest and most massive. It shines ten times brighter than the Sun, and the only reason we don't notice it is that it's so very remote. — *A History of the Universe in 100 Stars* (Quercus Press), p. 290, 2022.